# Scattering and Frequency Effects on Ultrasonic Velocities of Carbonates

**Nicola Tisato[1], Kyle T. Spikes[1], Nishank Saxena[2], Ronny Hofmann[2]**

[1]Department of Geological Sciences, Jackson School of Geosciences, The University of Texas at Austin

[2]Shell International Exploration & Production, Houston, TX

Corresponding author: Nicola Tisato (nicola.tisato@jsg.utexas.edu)

**Key Points:**

- Scattering of elastic waves
- Physical properties of carbonates
- Frequency-dependent velocities and attenuation

## Abstract

Seismic methods are key to subsurface imaging, and they rely on rock physics models that assign properties of interest from measured physical properties. However, assigning properties of interest, such as lithology, porosity, and permeability to subsurface domains requires solving a non-unique problem. Different combinations of measured physical properties can produce similar sets of properties of interest. Here we present and discuss benchtop measurements and numerical modeling of ultrasonic wave velocities in homogeneous and heterogeneous carbonate rocks. In heterogeneous rocks, the stress-induced variation of pore shapes and the presence of multiphase pore fluids affect the elastic wave velocities and are among the most invoked mechanisms to explain the observed variations of elastic wave velocities. Instead, we show that the scattering of elastic waves has a first-order effect on the velocities of the elastic waves and should be considered when applying rock physics models, at all scales, in carbonates, and in rocks that contain heterogeneities. Furthermore, we illustrate a laboratory method to measure frequency-dependent ultrasonic velocities (i.e., dispersion) and show that finite-difference modeling can reproduce the laboratory-observed dispersion, including the typical frequency shift produced by scatterers and dispersive media.



## Plain Language Summary

Observations of how fast elastic waves or vibrations travel in the subsurface have provided the foundation for what we know of our planet's interior. However, this method, called seismology, cannot directly provide information such as the type of rock or fluid at depth. Instead, we interpret elastic wave velocities to create maps of useful information, such as the presence of water at depth. Those interpretations, unfortunately, can lead to errors as similar variations of wave velocities can result from different reasons. This work shows that very common rocks with large pores can exhibit variable velocities as the frequency of the elastic wave varies. This phenomenon is well known and is called the scattering of elastic waves, but often is not interpreted as the reason for velocity variations. Instead, other mechanisms, such as the variation of pore shape, might be erroneously invoked. We show and discuss laboratory experiments and computer modeling affected by scattering, helping geoscientists interpret wave velocity to improve the imaging of the subsurface.


## 1 Introduction

This work presents laboratory measurements and numerical wave propagation results to understand the velocity dispersion due to the scattering of elastic waves in heterogeneous rocks (e.g., de Hoop, 1995; Snieder, 2002). Here, for simplicity, we refer to the "elastic wave scattering" as "scattering." We tested dry carbonate rocks that typically have a limited intrinsic attenuation (Adam et al., 2009), demonstrating that scattering is a primary source of dispersion in these rocks. A characteristic length-scale controls the scattering magnitude and the range of critical frequencies where the mechanism is active. In carbonates, the characteristic length scale or scatterer size (ds) is a function of the microstructures and pore-scale structures that are controlled by the grains and micrite making up the matrix, the diagenetic processes, and the formation of secondary porosity (Bosellini et al., 1995). In particular, the size, number, and spatial distribution of pores are the main causes of scattering as pores and solid matrix have a large contrast of elastic impedance (i.e., the product of density and wave velocity).

Much experimental work on carbonates aims to determine relationships between physical and elastic properties, most often as a function of effective pressure. Many physical properties are of interest as well as how they evolve under depositional and burial conditions. Examples include pore type, porosity, fluid type and saturation, composition, and diagenetic alteration. Pore type and rock microstructures and their links to elastic wave velocities have been studied extensively (e.g., Casteleyn et al., 2010, 2011; Lambert et al., 2006; Leger & Luquot, 2021; Regnet et al., 2019; Wang, 1997; Weger et al., 2009). Studies of how porosity forms and evolves include, for example by Anselmetti et al., 1997; Baechle et al., 2008; Carpenter et al., 2015; Eberli et al., 2003; Heydari, 2003; Rafavich et al., 1984; Verwer et al., 2008). Pore-fluid type, pore-space structure, and fluid saturation can also affect the velocity response of carbonates (Ludmila Adam et al., 2006; Clark & Vanorio, 2016; Ikeda et al., 2021; Pimienta et al., 2014; Rasolofosaon & Zinszner, 2003; Verwer et al., 2010). Mineralogy, such as calcite versus dolomite-bearing rocks, also present different elastic properties (Fabricius et al., 2010; Japsen et al., 2004; J. B. Regnet, David, et al., 2015; J. B. Regnet, Robion, et al., 2015; J.-B. Regnet et al., 2019; Røgen et al., 2005). Lastly, many authors have demonstrated the significant effects of diagenetic alteration on seismic velocities, particularly when diagenesis affects young sediments at shallow depths (e.g., Bemer et al., 2017; Makhloufi et al., 2013; Nader et al., 2016; Neveux et al., 2014).

Variations in elastic wave velocities, however, could result because of others reasons that could be misleading. Elastic wave velocities also depend on the frequency of the propagating waves. The phenomenon of frequency-dependent elastic wave velocities (dispersion) has been examined across a wide range of frequencies from the seismic-field scale (<100 Hz) to the sonic (~100Hz – 10 kHz) and ultrasonic (>20 kHz) bandwidths. Laboratory measurements on core samples require various techniques to cover the sub- to MHz bandwidth (e.g., Best et al., 1994; Peselnick & Outerbridge, 1961; Subramaniyan et al., 2014; Toksöz et al., 1981). Thus, broadband laboratory measurements require comparing ultrasonic transmission to resonant-bar and sub-resonance measurements to piece together velocity dispersion curves (e.g., Adam et al., 2009; Bourbié et al., 1987; Lozovyi & Bauer, 2019; Szewczyk et al., 2016; Tisato et al., 2021).

When samples are fluid-saturated, the dispersion may result from other mechanisms such as the wave-induced fluid flow (WIFF) acting at different critical frequencies that are also a function of the rock microstructures (Mavko et al., 2009). An arguably simpler scenario is to consider a limited set of dispersion mechanisms based on measurements of dry samples at ultrasonic frequencies. In such conditions, we can assume that the dispersion arises from the intrinsic anelasticity of the minerals making up the rock, the friction between grains, and scattering (e.g., Walsh, 1966; K. Winkler et al., 1979; K. W. Winkler & Nur, 1982). Conducting pulse transmission measurements at variable ultrasonic frequencies requires techniques beyond the normal practice in experimental rock physics (Birch, 1960). Typically, measurements on carbonates have been performed at a fixed nominal frequency, mainly dictated by the source signal and transducer characteristics (e.g., Kenter et al., 2007). The transducer, a piezoelectric crystal padded with different materials, controls the transmission of the propagating energy. It resonates at a central frequency when it is excited with a broadband signal. That broadband signal is a spike that contains frequencies up to tens of MHz, typically higher than the transducer resonating frequency (0.1–10 MHz). The signal frequency is held constant also for pragmatic reasons, such as comparing measurements performed during pressure or saturation cycling to simplify the experimental configuration. Therefore, this choice depends on the sensor and the design of the source signal, and the experiment.

Another aspect of the frequency-dependent scenario regards the rock sample. Scattering causes dispersion that is coupled with apparent attenuation in addition to intrinsic attenuation, which controls the frequency of the transmitted wavelet (Quan & Harris, 1997; Richards & Menke, 1983). In particular, the central frequency of the output signal will tend to be lower than the frequency of the input signal. Fabricius et al. (2010) discussed such an effect for dry and saturated carbonates. However, many publications do not compare input and output signal frequency content nor discuss the implication of such a change in signal frequency.

A possible solution to untangle scattering from intrinsic attenuation is to independently estimate scattering using analytical or numerical modeling. Analytical solutions for scattering, however, are typically limited to scatterers with simple geometries and low number density (e.g., Aki & Richards, 2009; Gritto et al., 1995; Johnson, 2018; Korneev & Johnson, 1996). On the other hand, numerical simulations can handle high number density scatterers with complex geometries and vary the dominant frequency of the source wavelet (Di Martino et al., 2022; Matsushima et al., 2020; Richards & Menke, 1983). Numerical simulations become powerful when performed on models that represent the real geometry and distribution of pores, such as those obtained with micro-computed tomography (μCT) (Andrä et al., 2013b, 2013a; Ikeda et al., 2021). Among the methods to simulate wave propagation, finite-differences (FD) (e.g., Bohlen, 2002; Saenger et al., 2004; Saenger & Bohlen, 2004) adapt well to μCT imagery. However, μCT images cannot be directly used in FD simulations. To create FD input parameter matrices, one or more intermediate steps – either involving or not segmentation – must be applied to assign physical properties of each μCT voxel (e.g., Goldfarb et al., 2022; Ikeda et al., 2020, 2021; Kerimov et al., 2020; Madonna et al., 2012; Saxena et al., 2019). Because scattering is mostly effective for wavelength to scatterer size ratios ($\lambda/ds$) around $2\pi$, the resolution of the μCT imagery becomes important to properly simulate scattering. For carbonates one can consider a typical minimum body wave velocity of 2000 m/s and a maximum testing frequency of 1.2 MHz, providing a minimum wavelength ($\lambda_{min}$) of 1.6 mm. Thus, a μCT resolution of 16 μm – typical for centimetric-sized samples - would be able to capture scatterers ~100 times smaller than the wavelength. For $\lambda/ds$~100 wave propagation can be approximated by effective medium theories (Mavko et al., 2009).

Here, we measured compressional and transverse wave (i.e., P and S waves) velocities at different ultrasonic frequencies in carbonate samples with different porosities and scatterer sizes. We used transducers producing enough energy over a wide bandwidth (0.2–2 MHz) and employed a variable input frequency (0.3–1 MHz) without changing sensors or technique. The same sensors were also able to detect waves in the source bandwidth. In addition to the laboratory measurements, we simulated the propagation of P and S waves at different frequencies (0.3–1.2 MHz) on segmented μCT models. According to the μCT resolutions, pore sizes, and employed wave frequencies we tested $\lambda/ds$ between ~2 and ~100. Such a range indicates that we have mainly tested Rayleigh scattering to effective medium conditions (Mavko et al., 2009). This work shows that in heterogeneous rocks, such as carbonates, variations of ultrasonic velocities – especially when source and transmitted wave frequencies are not thoroughly assessed - might result from scattering rather than variations of petrophysical properties.

The organization of the paper follows this structure. First are the descriptions of the samples. Next is the explanation of the techniques for the ultrasonic laboratory measurements, including calibration. The third component details the signal analysis of the waveforms and

147 amplitude spectra to determine arrival times and dominant frequencies, respectively. We then
148 present the steps for the numerical simulations. The results then demonstrate the similarity of the
149 dispersion between the laboratory measurements and simulated scenarios. A discussion then
150 amalgamates the results, along with explanations and implications. Finally, we provide
151 concluding remarks.

152

153 ## 2 Materials and Methods

154 ### 2.1 Samples

155 We performed measurements of ultrasonic wave velocities on five carbonate samples named
156 LSK068 (Rocherons Limestone), LSK062 (Edward Yellow Limestone), LSK014 (Indiana
157 Limestone), LSK050 (Buda Limestone), and LSK059 (Silurian Dolomite). These samples are a
158 set of outcrop rocks purchased from Korurek Industries (https://kocurekindustries.com/) ~38 mm
159 long and 25.4 mm in diameter cylinders. The porosity of each core was measured using a helium
160 pycnometer (our development). Table 1 reports sample dimensions, porosities, and abundances
161 of main minerals in the five samples according to X-ray diffraction analyses. All samples are
162 comprised mainly of calcite except LSK059, which is comprised of 99.1% dolomite. We used
163 micro-computed tomography (μCT) to study the internal structure of the rocks and obtain 3D
164 models of the core samples. According to Dunham (1962) and μCT images (fig. 1) we classified
165 the samples as mudstones and packstones.
166

| **Sample** | **LSK068** | **LSK062** | **LSK014** | **LSK050** | **LSK059** |
|---|---|---|---|---|---|
| **Length (L±ΔL) (mm)** | 38.14±0.02 | 38.18±0.03 | 38.20±0.07 | 38.19±0.06 | 38.23±0.02 |
| **Diameter (mm)** | 25.4 | 25.4 | 25.4 | 25.4 | 25.4 |
| **Φ (%)** | 3.0 | 26.0 | 21.0 | 8.0 | 11.0 |
| **Quartz (%)** | 0.4 | 0.6 | 1.1 | 1.4 | 0.5 |
| **Calcite (%)** | 99.4 | 98.3 | 98.6 | 97.1 | 0.2 |
| **Dolomite (%)** | 0.2 | 1.0 | 0.3 | 0.2 | 99.1 |
| **Other minerals (%)** | 0.0 | 0.1 | 0.0 | 1.3 | 0.2 |
| **Classification** | Mudstone | Packstone | Packstone | Mudstone | Packstone |

167 *Table 1. Core sample properties.*

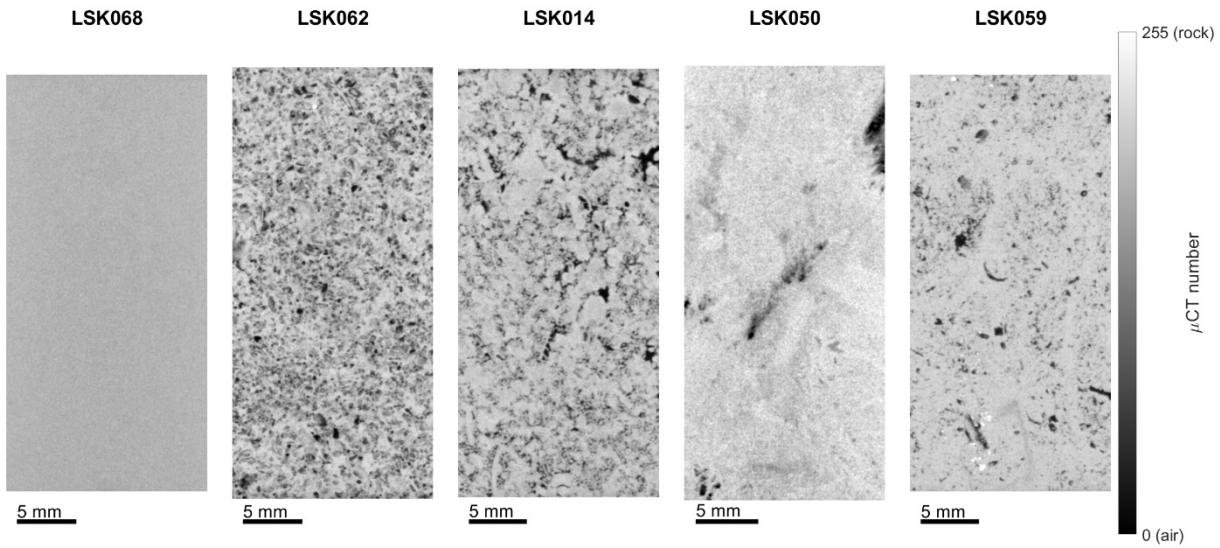


*Figure 1. 2D slices of the 3D μCT volumes of the five core samples. Grain sizes and porosity dictated the mudstone and packstone classifications. LSK068 is homogeneous, and the others are more heterogeneous.*

## 2.2 Ultrasonic velocities

***Laboratory data acquisition***

Ultrasonic P and S velocities were measured using a modified version of the pulse transmission method (Birch, 1960) and by dividing the sample length by the travel time of the ultrasonic wave through the core specimens. Figure 2 shows the experimental setup. The classic pulse transmission method drives the ultrasonic source with a broadband input signal generated by a pulse generator (Tisato & Marelli, 2013). Consequently, the source elastic wave has a frequency close to the resonance frequency of the transducers, typically between 0.1 and 10 MHz, depending on the transducers.

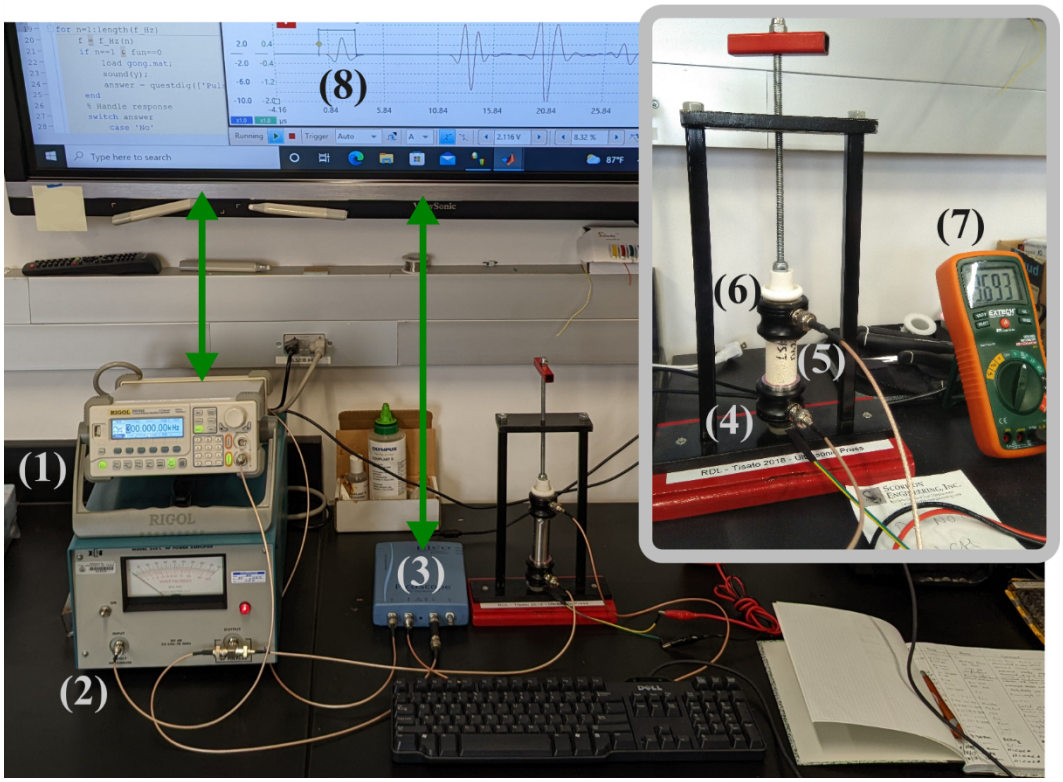


*Figure 2. Laboratory setup. The Matlab script running on the computer controls via USB the function generator (1), the signal generated by the function generator feeds into a linear amplifier (2) whose output signal is recorded by channel C of the digital oscilloscope (3), and powers the ultrasonic source (4). Channel A of the oscilloscope records the function generator trigger signal. The sample (5) is compressed between the source and the receiver (6) using a screw press. The normal force applied to the measuring column is measured by a load cell and a digital multimeter (7). The signal generated by the receiver is recorded by channel B of the oscilloscope, and the acquisition software (8), which is also controlled by the Matlab script.*

In the present work, we drove the ultrasonic source using an arbitrary waveform generator (Rigol DG1022) and a linear RF power amplifier (ENI 240). Such a device allows producing ultrasonic waves at a specific frequency and with a known wavelet. The ultrasonic sources and receivers are pairs of Olympus V102 and V152 piezoelectric transducers to generate and detect P and S waves, respectively. According to the frequency spectra (see Figure S1), our transducers can produce ultrasonic waves between ~0.2 and 2 MHz. Calibration did confirm that our transducers can produce and detect elastic energy in the measuring bandwidth, i.e., 0.3 to 1 MHz.

During testing, we clamped the sample between a pair of transducers using ultrasonic couplant gels (Olympus couplant D and SWC-2 for P and S waves, respectively) to improve energy transmission at the transducer-sample interfaces. The normal force was measured using a resistive load cell and kept around 360 N during testing. A Matlab script controls the function generator producing a Ricker wavelet with amplitude 0.25 Volts and nominal frequency ($f_n$) varying between 0.3 and 1 MHz. The ENI 240 amplifies the signal of 50 dB, i.e., increases the signal amplitude by 316 times and drives the ultrasonic source. This power signal is called "input" and recorded by channel C of the oscilloscope (Picoscope 4424) through a resistive

voltage divider that attenuates the signal by 40 dB. The transducer on the top of the sample sensed the transmitted wave ("output") that was recorded by channel B of the oscilloscope. The Matlab script also controls the data acquisition by managing the acquisition software (Picoscope 6.14). The function generator and the oscilloscope were time-synchronized by connecting the external trigger of the function generator to channel A of the oscilloscope. All channels were acquired with a vertical resolution of 12 bits, a sampling rate of 40 MHz for a total time of 50 μs.

For each core sample, we acquired ultrasonic velocities at eight different nominal frequencies. First, we acquired input, output, and trigger signals for increasing $f_n$ between 0.3 and 1 MHz in steps of 0.1 MHz. Then, we acquired input, output, and trigger signals for decreasing $f_n$ between 0.9 and 0.3 MHz in steps of 0.1 MHz (i.e., frequency cycling). In total, we acquired ultrasonic velocities at fifteen nominal frequency steps. At each $f_n$ step, we repeat the acquisition of the transmitted wavelet 32 times to later perform stacking and improve the signal-to-noise ratio. Single traces were saved as comma-separated-value (csv) files.

***Data analysis***

We developed and used Matlab scripts to analyze input and output signals to determine i) travel times via picking and ii) the frequency content of the source and transmitted signals. For laboratory data, such analysis is performed on stacked signals following these steps.

- The input signal is normalized by the amplitude of the first trough, i.e., "input first trough" (IFT) as labeled in Figure 3. Hereafter, the term "input signal" refers to the normalized input signal;
- On P waves, specific peaks (PSP) are identified on the output signal using the Matlab built-in function *findpeaks* with parameters: i) minimum peak distance of $1/(2\,f_n)$ and ii) minimum peak prominence equal to a fourth of the signal amplitude standard deviation. As P wave input and output signals have the same polarity, the output signal is normalized by the amplitude of the trough aftergoing the first PSP, also called "output first trough" (OFT). Hereafter, the term "output signal" refers to the normalized output signal;
- On S waves, specific peaks (SSP) are identified on the output signal using the Matlab built-in function *findpeaks* with parameters: i) minimum peak distance of $1/(2\,f_n)$ and ii) minimum peak prominence equal to the maximum of the output signal multiplied by a coefficient chosen between 0.3 and 0.5. Such a coefficient varied among samples and is empirically determined until the algorithm locates the first S wave peak. Because S wave input and output signals have opposite polarities, the output signal is normalized by the amplitude of the first peak and then inverted. In such a way, the first SSP becomes the "output first trough" (OFT). Hereafter, the term "output signal" refers to the normalized and inverted output signal;
- We define the *ISS* as the part of input signal that has an amplitude ranging –0.03 to –0.3 and lays between the input zero-crossings preceding the IFT (thick gray line segments in Figure 3);
- We define the *OSS* as the output signal that has vertical values ranging from -0.03 to -0.3 and lays between the output zero-crossings preceding the OFT (thick red line segments in Figure 3);

The travel time (*tt*) was estimated as:

$$tt = ttO - ttI,$$

$$ttO = \frac{\sum_{i=1}^{N} t_{OSS\,i}}{N}, \quad \text{eq. 1}$$

$$ttI = \frac{\sum_{i=1}^{N} t_{ISS\,i}}{N},$$

where *N* is the number of recorded samples in the *ISS* and *OSS,* and $t_{OSS\,i}$ and $t_{ISS\,i}$ are the *ith* sample times within the *ISS* and *OSS*. Because S wave output signals are mixed with a converted P wave signal (Sp), S wave travel time is first estimated using eq. 1 and then refined by manual picking.

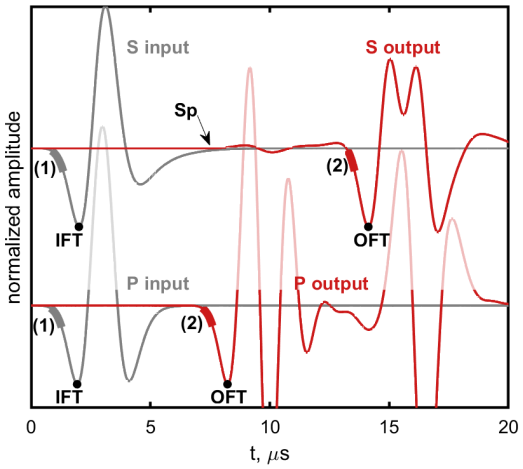


*Figure 3. Examples of picking for an S and a P-wave, top and bottom traces, respectively. (1) and (2) indicate the input (ISS) and output (OSS) selected signals. Travel times are estimated by measuring the time distance between ISS and OSS. Sp is the P wave arrival due to a S to P wave conversion.*

The uncertainty on *tt* is defined by a lower ($\Delta tt^-$) and upper ($\Delta tt^+$) bound:

$$\Delta tt^- = \min_{i=1,2,\ldots N}(t_{OSS\,i} - t_{ISS\,i}) - tt - \frac{1}{f_s},$$

$$\Delta tt^+ = \max_{i=1,2,\ldots N}(t_{OSS\,i} - t_{ISS\,i}) - tt + \frac{1}{f_s}, \quad \text{eq. 2}$$

where $f_s$ is the sampling rate.

The frequency content of the input and the output signals is evaluated by performing the fast Fourier transform on the signal and fitting the amplitude spectra with a skewed Gaussian function (Azzalini, 1985):

$$g(f) = \frac{A}{\omega\sqrt{2}} e^{\frac{-(f-\xi)^2}{2\omega^2}} \frac{1}{2}\left(1 + erf\left(\frac{f-\xi}{\alpha\sqrt{2}}\right)\right), \quad \text{eq. 3}$$

Where *A*, $\omega$, $\xi$ and $\alpha$ are the fitting parameters, and *f* is frequency. The mean frequency of the signal is defined as :

$$\bar{f} = \xi + \omega\delta\sqrt{\frac{2}{\pi}}, \quad \text{eq. 4}$$

Where $\delta$ is:

$$\delta = \frac{\alpha}{\sqrt{1+\alpha^2}}, \quad \text{eq. 5}$$

The mean frequency standard deviation is calculated as:

$$\sigma = \omega\sqrt{\left(1 - \frac{2\delta^2}{\pi}\right)}, \quad \text{eq. 6}$$

We defined $f_i$ and $f_o$ as the $\bar{f}$ calculated for the input and the transmitted (output) wave, respectively. To evaluate the input to transmitted frequency shift that is typical of dispersive media (e.g., Aki & Richards, 2009; Quan & Harris, 1997; Richards & Menke, 1983), we calculated the frequency shift coefficient ($\Delta f$) for each experiment. The frequency shift coefficient ($\Delta f$) was calculated on numerical and laboratory experiments on samples LSK068, LSK062, LSK014 and LSK050 as:

$$\Delta f = \frac{1}{M}\sum_{m=1}^{M}\frac{f_{o\,m}}{f_{i\,m}}, \text{eq. 7}$$

Where $m$ is m*th* measurement among the $M$ performed on the sample: $N$ is 8 and 15 for numerical and laboratory experiments, respectively. A $\Delta f$ of around one indicates that, on average, $f_o$ is similar to $f_i$, typical of elastic media. On the other hand, a $\Delta f$ below one indicates that, on average, $f_o$ is lower than $f_i$, which is typical of dispersive media.

*Calibration*

We performed a calibration to correct the travel times for the delay introduced by the transducer pairs. Such a calibration was performed independently for P and S waves. For both wave types, we measured travel times at five nominal frequencies ($f_n$ = 0.2, 0.4, 0.6, 0.8, and 1 MHz) on four stainless steel (AISI 304) cylinders with a diameter of 25.4 and lengths of 38.1, 50.8, 63.43, and 76.20 mm. Thus, we obtained 40 travel times, i.e., one for i) each wave type, ii) nominal frequency, and iii) sample length. Figure 4 shows two examples of calibration wavelets and frequency contents.

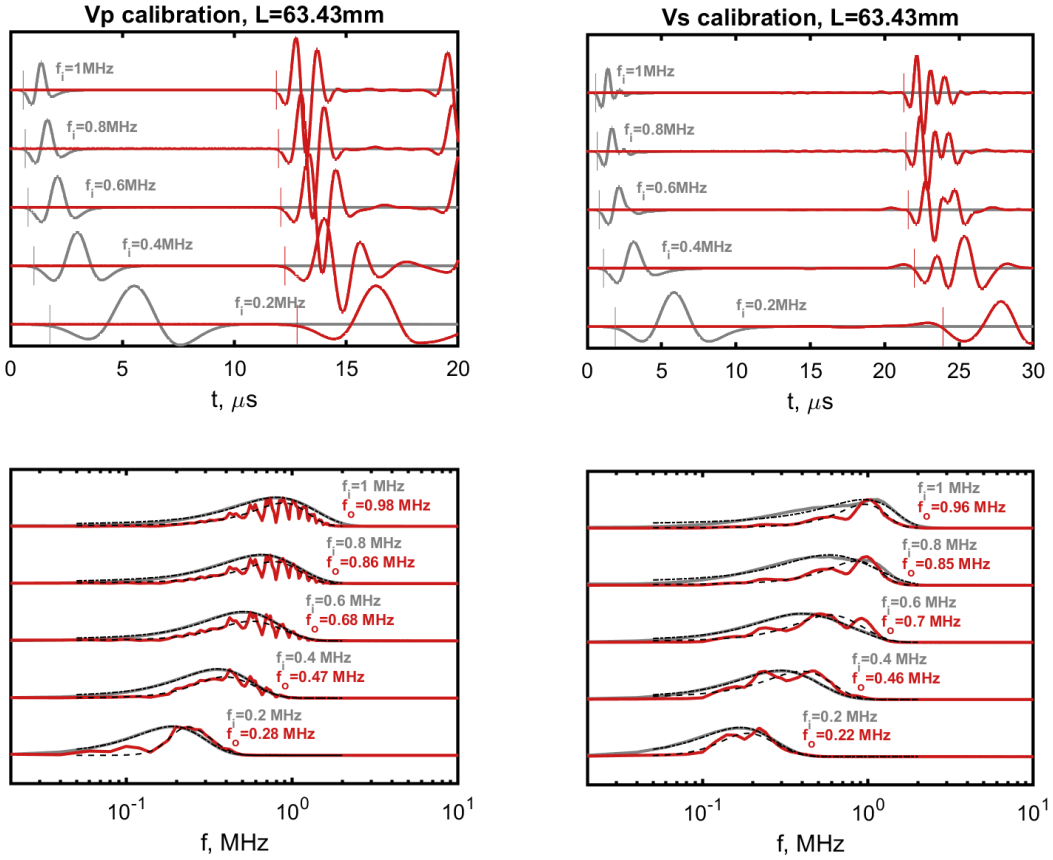


*Figure 4. On top, input and output signals for P and S waves and five different nominal frequencies. The sample is a stainless steel cylinder of length (L) 63.43 mm used for calibration. Vertical gray and red lines indicate input and output picking, respectively. The travel time is calculated as the time distance between the input and output picking. On the bottom, the amplitude of the signals Fourier transforms. Amplitude spectra are fit with skewed Gaussians (Azzalini, 1985), and mean frequencies of input and output signals are shown as $f_i$ and $f_o$, respectively.*

For both P and S-waves, we grouped travel times according to the nominal frequency ($f_n$) and obtained five linear fitting curves describing travel times as a function of sample lengths (i.e., one for each frequency). The five intercepts of these linear fits represent the travel times extrapolated to a zero-length sample, effectively representing the delays introduced by the transducer pairs at each frequency (See Figure S2). Intercepts on the frequency-travel time plane were fit with a second-order polynomial:

$$\Delta t_{p,s} = a\, f_n^{\,2} + b\, f_n + c \qquad \text{eq. 8}$$

Where $\Delta t$ is the delay in general and $\Delta t_p$ $\Delta t_s$ for P and S-waves, respectively.

*Wave velocities*

Velocities in rock samples are calculated as $V^{+\Delta V^+}_{-\Delta V^-}$:

$$V = \frac{L}{tt - \Delta t} \qquad \text{eq. 9}$$

Where $L$ is the sample length, $\Delta L$ is the sample length uncertainty and $\Delta V^{+}$, $\Delta V^{-}$ are the positive and negative uncertainties calculated as:

$$\Delta V^{+,-} = V\sqrt{\left(\frac{\Delta L}{L}\right)^2 + \left(\frac{tt - \Delta t}{\Delta tt^{-,+}}\right)^2} \qquad \text{eq. 10}$$

.

## 2.3 Micro-computed tomography, segmentation, and numerical simulation of wave propagation

Micro-computed tomographies (μCT) were acquired at resolutions (dh) ranging between 30.75 and 32.20 μm per voxel using a Zeiss Versa 520 3D X-ray microscope at a voltage of 80kV. The images were acquired using ~2000 projections and corrected for beam hardening. We saved μCT imagery values with 8 bits resolution (i.e., 0-255 levels) and performed segmentation of such values to binarize voxels into three phases (0, 1, and 2). These three phases represent three materials: air, porous rock, and solid mineral. Air and mineral represent extremes; instead, the "porous rock" – i.e., phase 1 - represents unresolved micro-porosity, e.g., micrite (e.g., Saenger et al., 2016); i.e., “microporosity” means porosity with pore bodies smaller than the image resolution of the μCT imagery. A machine learning segmentation method (IPSDK Explorer https://www.reactivip.com/) was used to segment the μCT images. This kind of pixel-based segmentation uses different feature maps (volumes) and a random walker in combination with a set of hand-labeled phase identifications. The algorithm segments the image based on the CT number and textural features, as shown in figure 5 by the overlapping histograms.

Figure 5 shows histograms of voxel values and assigned phases for each sample, along with two-dimensional slices of segmented samples. Segmented sample LSK068 comprises only phase 2, while the other samples contain variable quantities of phase 0 and 1. For samples LSK062, LSK014, LSK050, and LSK059, phase 0 represents 0.6 to 2.9% of the total volume, while porosities range between 8 and 26% (Table 1). On the other hand, phase 1 in those samples represents a volume between 7.9 and 47.4% of the total volume.

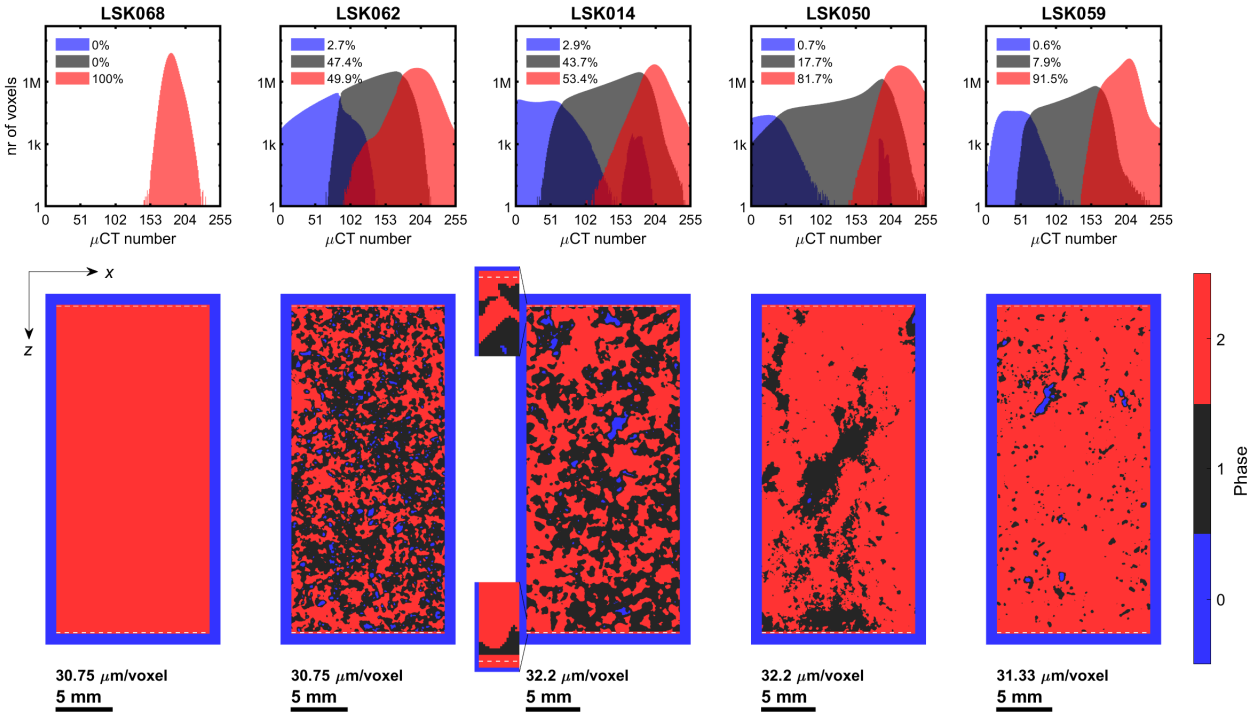


*Figure 5. On the top, histograms report μCT value distributions and percentages of assigned phases for the five samples. On the bottom, two-dimensional slices through the five segmented samples. Samples are padded with air to create ~zero stress boundaries. The colorbar indicates the color coding for each phase. White dashed lines indicate the location of sources and receivers for numerical modeling.*

We simulated laboratory experiments on four samples by simulating wave propagation on μCT derived models. First, for each model, we extracted a parallelepiped of dimensions 436x436x926 voxels along x, y, and z-direction, respectively. We added 436x436x5 voxels made of phase 2 to the sample ends to create solid paddings preventing sources and receivers from being placed inside pores. Sources and receivers loci were chosen on a regular grid spaced 20 voxels along two x-y planes inside the end sample paddings. Thus, sources and receivers were 930 voxels apart along the z-axis. Finally, we added 32 voxels on each side of the model. Each final model was then 500x500x1000 voxels (Figure 5).

We assigned density, bulk and shear modulus to each final model voxel according to voxel phases. Assigned properties and derived P and S wave velocities for each phase are reported in Table 2. The properties of phases 0 and 2 are the properties of air and calcite, respectively (Mavko et al., 2019), while the properties of phase 1 have been calculated assuming a porous rock phase (micrite) with 30% porosity and a modified Voigt-Reuss-Hill average with critical porosity of 60% (Goldfarb et al., 2022; Mavko et al., 2019).

| Phase | 0<br>Air | 1<br>Porous Rock | 2<br>Solid Rock |
|---|---|---|---|
| **K (GPa)** | 1.12E-04 | 17.5 | 70 |
| **G (GPa)** | 0 | 7.5 | 30 |
| **ρ (kg/m$^3$)** | 1 | 1897 | 2710 |
| **$V_p$ (m/s)** | 335 | 3807 | 6371 |
| **$V_s$ (m/s)** | 0.0 | 1988 | 3327 |

*Table 2. Physical properties assigned to the segmented μCT models.*

We used the code SOFI3D (Bohlen, 2002) to simulate the propagation of elastic waves in final models using a non-staggered grid. SOFI3D uses a time-explicit finite difference method to calculate the displacement at each voxel. Simulations resembled the laboratory transmission method as we forced displacement at source locations using a Ricker wavelet:

$$r(t) = (1 - 2\tau^2)e^{-\tau^2} \quad \text{eq. 11}$$

where $\tau = \pi f_c \left(t - \frac{3}{2f_c} - t_d\right)$, $f_c$ is the corner frequency and $t_d = -\frac{4}{10f_c}$, which is the delay time.

The plane elastic wave generated at the source locations propagated through the medium along the z-axis and reached the receivers that collected displacement signals in the three directions. Receiver signals were averaged to produce single seismograms along each direction, imitating the signal collected by piezoelectric crystals in the laboratory. We performed two simulations for each sample: one for measuring P-wave velocity where source displacement was parallel to the z-axis and one for estimating S-wave velocity in which source displacement was parallel to the x-axis. For P and S-wave experiments, we analyzed z and x displacement seismograms, respectively. Finally, the wave speed was calculated as the ratio between the source-to-receiver distance (i.e., 930·dh) and the time that the elastic wave took to travel across the sample. Travel times are estimated using the same methods described previously to estimate travel times for laboratory experiments.

To analyze our results in terms of the wavelength (λ) to scatterer size (ds) ratio (λ/ds), we estimated the pore size distribution (PSD) of each sample from the μCT imageries. The analyses were performed on the portion of datasets representing the rock, i.e., we eliminated the top and bottom calcite pads and the air borders obtaining 3D volumes of 927x437x437 voxels. We used the continuous 3D Pore Size Distribution function of the Xlib plugin of ImageJ (Münch & Holzer, 2008), considering three different pore spaces: the voxels represented by i) phase 0, ii) phase 1, and iii) phase 0 and 1 merged. Such a tool calculates the pore radii distribution by fitting spheres with variable diameters within the pore space. We selected to search within diameters ranging between 2·dh and 100·dh.

## 3 Results

Raw data include 15 laboratory and 8 numerical ultrasonic wavelets for each sample. For simplicity, results are grouped first for sample LSK068 for both the laboratory measurements and numerical simulations and then for sample LSK062. Those two samples, respectively,

exhibit little and significant dispersion. We report the results for samples LSK014, LSK050, and LSK059 in the supporting information as they would sound redundant to those of samples LSK068 and LSK062. Data are expressed as waveforms, amplitude spectra, and Vp, Vs, and Vp/Vs as a function of frequency.

Figure 6a includes normalized waveforms that correspond to different input frequencies. Time is in microseconds. Input frequencies ($f_i$) are displayed in the figure from 0.3 MHz at the bottom to 1 MHz at the top. Four waveforms are plotted and grouped in two pairs for each frequency: the gray and its superimposed black dashed line are input signals, whereas the red and its superimposed waveform are output signals. For both input and output waveforms, solid and dashed lines are signals for the frequency cycle from 0.3 up to 1 MHz, and from 1 down to 0.3 MHz, respectively. The envelopes of the input waveforms are easily seen in the outputs with little change in the phase. Also included are vertical tick marks that denote *ttI* and *ttO*. Figure 6b contains the amplitude spectra for each waveform of Figure 8a. The color scheme is the same as in Figure 6a, i.e., gray and overlapping black dashed lines indicate input waves for upgoing and downgoing frequencies, respectively; red and overlapping black dashed lines indicate transmitted waves for upgoing and downgoing frequencies, respectively. Also plotted in panel b are diamonds and thick overlain segments of the amplitude spectra representing $\bar{f}$ and $\pm\sigma$ of the respective panel a signals.

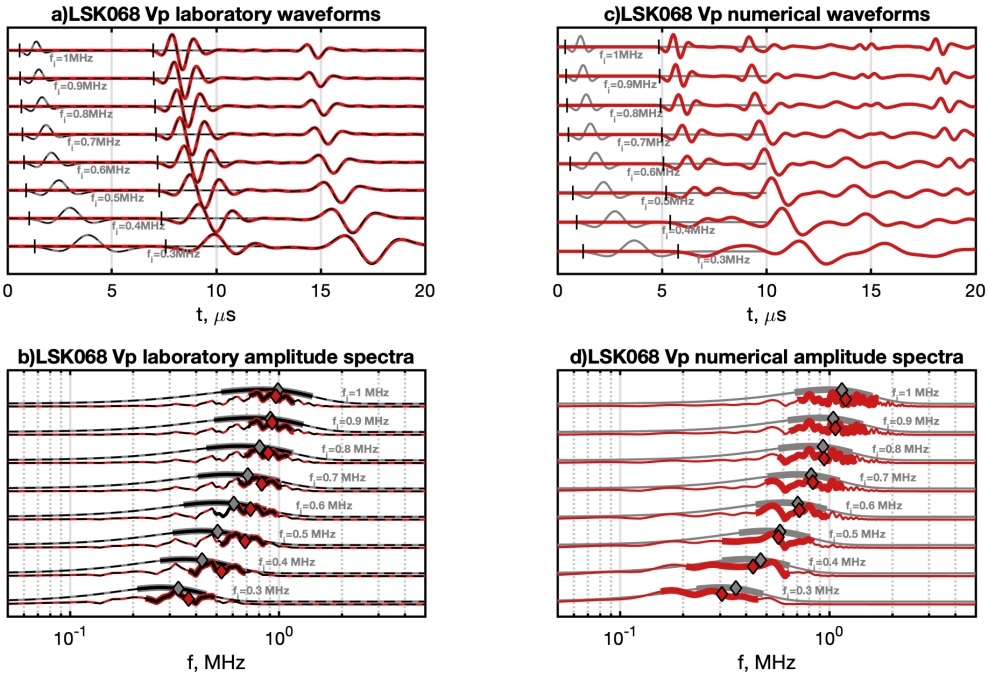


*Figure 6. a) Plot of laboratory P-wave waveforms for sample LSK068. Input frequencies ($f_i$) of the Ricker source signals are indicated in the text. The gray waveforms are the input signals for frequencies increasing from 0.3 to 1 MHz, and the overlain dashed black are the input signals for frequencies decreasing over that range. Red and their overlying dashed black waveforms are the transmitted waves. Those colors correspond, respectively, to the up- and down-going frequency cycling. b) Amplitude spectra for the waveforms in a) using the same color scheme. Diamonds and thick line segments correspond to $\bar{f}$ and $\pm\sigma$, respectively. c) P-wave waveforms*

*from numerical simulations for sample LSK068. Gray corresponds to input and red to transmitted signals. No black dashed lines are present because numerical simulations were performed only for the increasing frequency cycle. d) Amplitude spectra for the waveforms in c) using the same color designations as well as diamonds and thick lines for $\bar{f}$ and $\pm\sigma$, respectively. In panels a) and c), the distance between pairs of black vertical ticks on each wavelet corresponds to the travel time (tt).*

Figure 6c contains the waveforms, and 6d contains the amplitude spectra for the P-wave numerical simulations for sample LSK068. In Figure 6c, the input wavelets are in gray, and the observed waveforms are in red. No frequency cycling was necessary for these simulations, so only one set of inputs and observations are displayed. Waveforms correspond to frequencies from 0.3 to 1 MHz, and the black tick marks indicate *ttI* and *ttO*. Amplitude spectra in Figure 8d correspond to the inputs and outputs (i.e., gray and red), respectively. Diamonds and thick lines mark $\bar{f}$ and $\pm\sigma$ to each spectrum, respectively.

Figure 7 contains the Vs wavelets and amplitude spectra for sample LSK068, both laboratory and numerical experiments. Panel layouts, color schemes and symbols (i.e., ticks, diamonds and thick lines) have the same meaning as those in Figure 6.

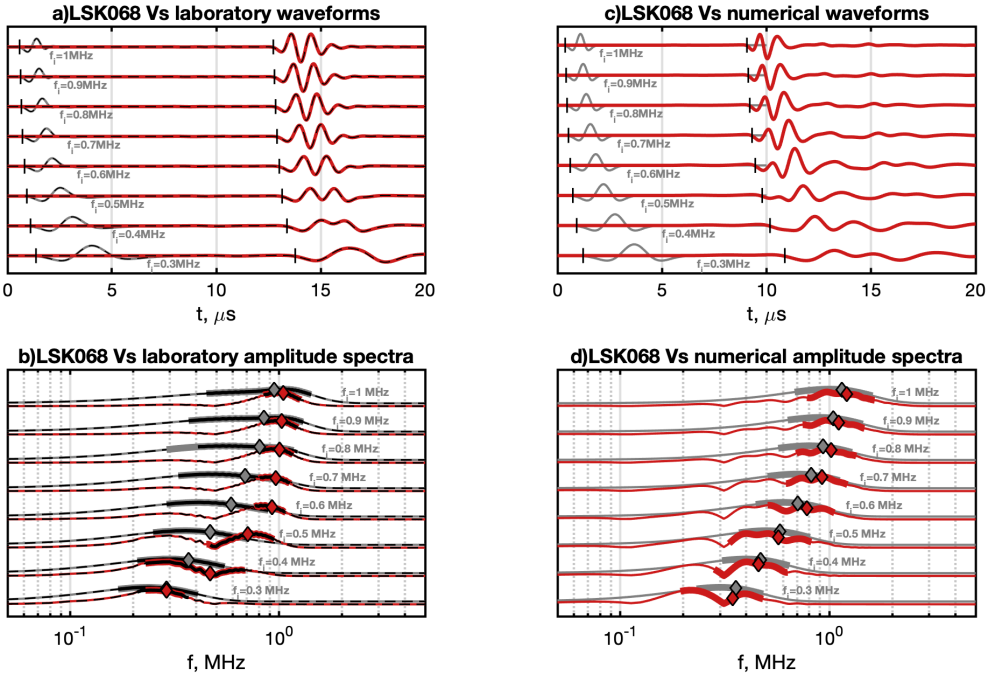


*Figure 7. a) Laboratory S-wave waveforms for sample LSK068. Input frequencies ($f_i$) of the Ricker source signals are indicated in the text. The gray waveforms are the input signals for frequencies increasing from 0.3 to 1 MHz, and the overlain dashed black are the input signals for frequencies decreasing over that range. Red and their overlain dashed black waveforms are the output waveforms for the up- and down-going frequency cycling, respectively. b) Amplitude spectra for the waveforms in panel a using the same color scheme. Diamonds and thick line segments correspond to $\bar{f}$ and $\pm\sigma$, respectively. c) S-wave waveforms from numerical*

*simulations for sample LSK068. Gray corresponds to input and red to output signals. No black dashed lines are present because numerical simulations were performed only for the increasing frequency cycle. d) Amplitude spectra for the waveforms in c) using the same color designations as well as diamonds and thick lines for $\bar{f}$ and $\pm\sigma$, respectively. In panels a) and c), the distance between pairs of black vertical ticks on each wavelet corresponds to the travel time (tt).*

Velocities as a function of frequency for LSK068 are in Figure 8; from panel a to panel c are compressional velocities (Vp), shear velocities (Vs), and compressional to shear velocities ratios (Vp/Vs), respectively. Diamonds and circles correspond to laboratory and numerical experiments, respectively. Plots for Vp and Vs contain two sets of frequencies. In gray are the velocities as a function of $f_i$, and in red are the velocities as a function of $f_o$. Error bars are equal to $\Delta V^{+,-}$ (eq. 10). Error bars on the frequency ($\pm\sigma$) are plotted on the amplitude spectra but not repeated in the crossplots. We calculated a velocity for each wavelet pair (i.e., input and output waveform) shown in Figure 6a, 6b, 7a, and 7b. Pairs are formed by picking velocities measured at the same $f_i$. The minimum to maximum Vp range is about 100 m/s, and the Vp values all fall above 6200 m/s. The range of Vp is within the error of the picked velocities, so this sample shows little velocity dispersion for Vp for the laboratory data. Simulated velocities are greater than laboratory ones, but the amount of dispersion is relatively small, and of the same order as the laboratory data and concentrated at the lowest frequencies (~0.3 MHz).

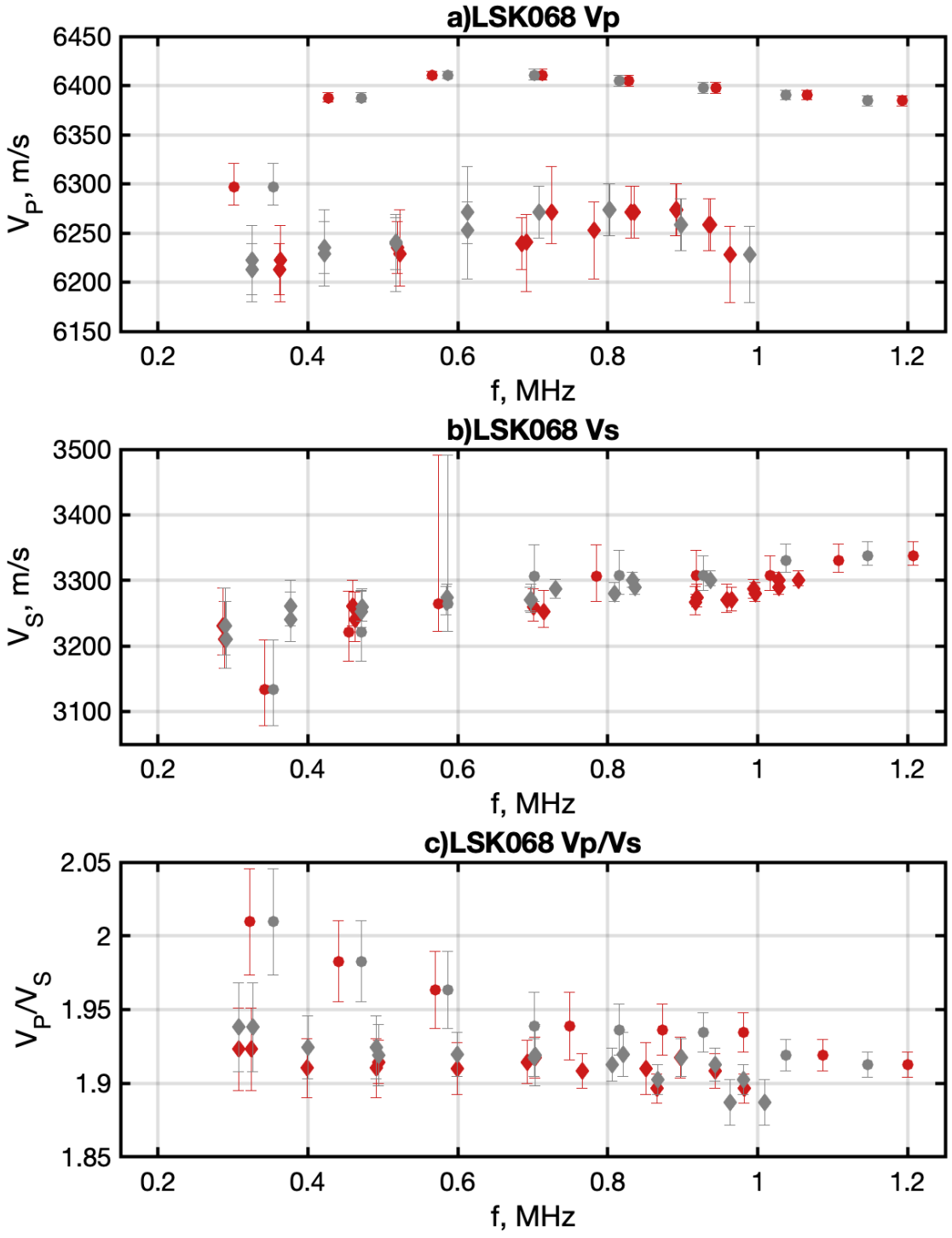


*Figure 8. Panel a and b are sample LSK068 frequency-dependent Vp and Vs, respectively. Diamonds and circles indicate laboratory and numerical measurements, respectively. Red and gray markers have frequencies equal to $f_o$ and $f_i$, respectively. Errorbars have magnitues equal*

494 *to $\Delta V^{+,-}$. The overall velocity range is about 100 m/s for both laboratory and numerical*
495 *experiments. The numerical experiment at the lowest frequency might be affected by a near-field*
496 *effect. Considering the indicated errors, this sample shows little observable dispersion. Vs*
497 *exhibits some dispersion, but very little considering the indicated errors Vs are within 150 m/s.*
498 *Lastly in panel c are the frequency-dependent Vp to Vs ratios (Vp/Vs) that are calculated for*
499 *each pair of Vp and Vs points measured at the same $f_i$. Vp/Vs frequencies are calculated as the*
500 *average of the frequencies of point pairs. Error bars on Vp/Vs are the RMS average of the error*
501 *bars on Vp and Vs point pairs.*
502
503 The overall Vs dispersion is ~100 m/s, so little Vs dispersion is present given the size of the error
504 bars for the laboratory data. The numerical values (circles) show similar velocity values and
505 range of dispersion to the laboratory results.
506
507 Last in Figure 8c are Vp to Vs ratios (Vp/Vs) as a function of frequency. Vp/Vs are calculated
508 for pairs or measurements (i.e., 1 Vp and 1 Vs) that have been measured at the same $f_i$. Each
509 point frequency is calculated as the average of the frequencies of the Vp and Vs points in the
510 pair. Error bars were computed using the root-mean-square (RMS) calculation that combined the
511 errors of the Vp and Vs points in the pair. All values of Vp/Vs exceed the minimum of $\sqrt{2}$ for
512 isotropic materials, are fairly constant (~1.9) for laboratory measurements over the frequency
513 range and decrease from 2 to 1.9 within the frequency interval for numerical experiments.
514
515 **Sample LSK062**
516
517 The results for sample LSK062, measured at the same $f_i$ of LSK068, are contained in the next
518 three figures (i.e., 9, 10 and 11). Figures 9 and 10 include wavelets and spectra for Vp (Figure 9)
519 and Vs (Figure 10), respectively. Data are presented in the same way as in Figure 6 and 7. Panels
520 a and b contain waveforms and relative spectra of laboratory measurements. Panels c and d
521 include waveforms and relative spectra of numerical experiments. At $f_i$ equal and less than 0.5
522 MHz, a relatively small shift between $f_i$ and $f_o$ is present. However, above 0.5 MHz, $f_c$ is
523 noticeably lower than $f_i$ (i.e., notice the divergence of gray and read diamonds as $f_i$ increases).
524 Clear first arrivals are apparent in the waveforms (vertical tick marks in a and c).
525

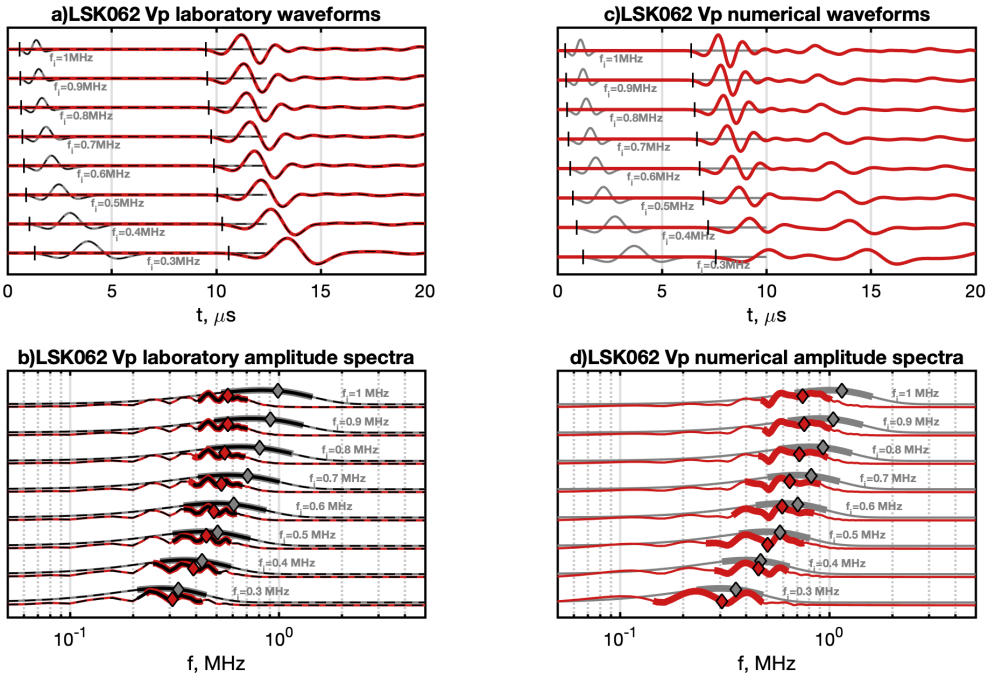


*Figure 9. a) Plot of laboratory P-wave waveforms for sample LSK062. Input frequencies ($f_i$) of the Ricker source signals are indicated in the text. The gray waveforms are the input signals for frequencies increasing from 0.3 to 1 MHz, and the overlain dashed black are the input signals for frequencies decreasing over that range. Red and their overlying dashed black waveforms are the transmitted waves. Those colors correspond, respectively, to the up- and down-going frequency cycling. b) Amplitude spectra for the waveforms in a) using the same color scheme. Diamonds and thick line segments correspond to $\bar{f}$ and $\pm\sigma$, respectively. c) P-wave waveforms from numerical simulations for sample LSK062. Gray corresponds to input and red to transmitted signals. No black dashed lines are present because numerical simulations were performed only for the increasing frequency cycle. d) Amplitude spectra for the waveforms in c) using the same color designations as well as diamonds and thick lines for $\bar{f}$ and $\pm\sigma$, respectively. In panels a) and c), the distance between pairs of black vertical ticks on each wavelet corresponds to the travel time (tt).*

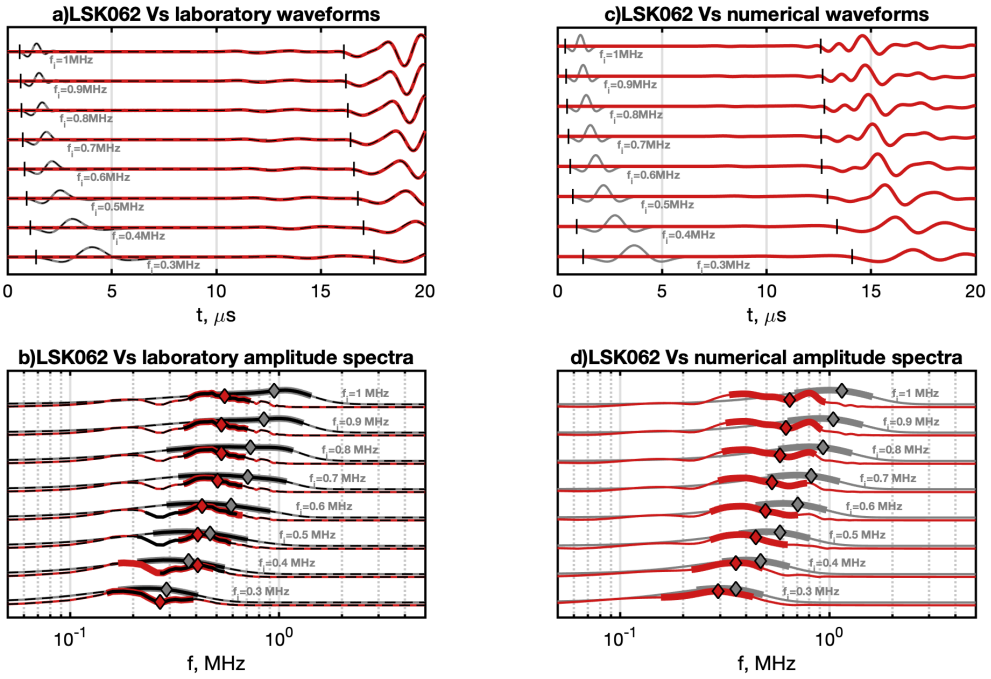


*Figure 10. a) Plot of laboratory S-wave waveforms for sample LSK062. Input frequencies ($f_i$) of the Ricker source signals are indicated in the text. The gray waveforms are the input signals for frequencies increasing from 0.3 to 1 MHz, and the overlain dashed black are the input signals for frequencies decreasing over that range. Red and their overlying dashed black waveforms are the transmitted waves. Those colors correspond, respectively, to the up- and down-going frequency cycling. b) Amplitude spectra for the waveforms in a) using the same color scheme. Diamonds and thick line segments correspond to $\bar{f}$ and $\pm\sigma$, respectively. c) S-wave waveforms from numerical simulations for sample LSK062. Gray corresponds to input and red to transmitted signals. No black dashed lines are present because numerical simulations were performed only for the increasing frequency cycle. d) Amplitude spectra for the waveforms in c) using the same color designations as well as diamonds and thick lines for $\bar{f}$ and $\pm\sigma$, respectively. In panels a) and c), the distance between pairs of black vertical ticks on each wavelet corresponds to the travel time (tt).*

Plots of the frequency-dependent Vp and Vs values for this sample are in Figures 11a and 11b, respectively. Data are presented using the same color scheme and markers as Figure 8. The Vp and Vs values are noticeably slower for this sample relative to LSK068. The dispersive behavior of Vp and Vs is evident by observing how the velocities indicated by red points and diamonds ($f_o$) and gray points and diamonds ($f_i$) increase along frequency. Laboratory P velocities increase of about 250 m/s over the frequency range, which exceeds the size of the error bars. Simulations (circles) show similar behavior in terms of dispersion magnitude and frequency range, but the numerical velocities are faster than the measured ones. For Vs, a dispersion of about 150 m/s is present over a narrow frequency range of 0.3–0.55 MHz (red diamonds), and simulations (circles) show a similar pattern. Finally, 11c contains Vp to Vs ratios (Vp/Vs) for measured (diamonds) and simulated values (circles) expressed as a function of $f_i$ (gray) and $f_o$ (red). The

laboratory and numerical Vp/Vs values do not match exactly, but the dispersion behavior is similar.

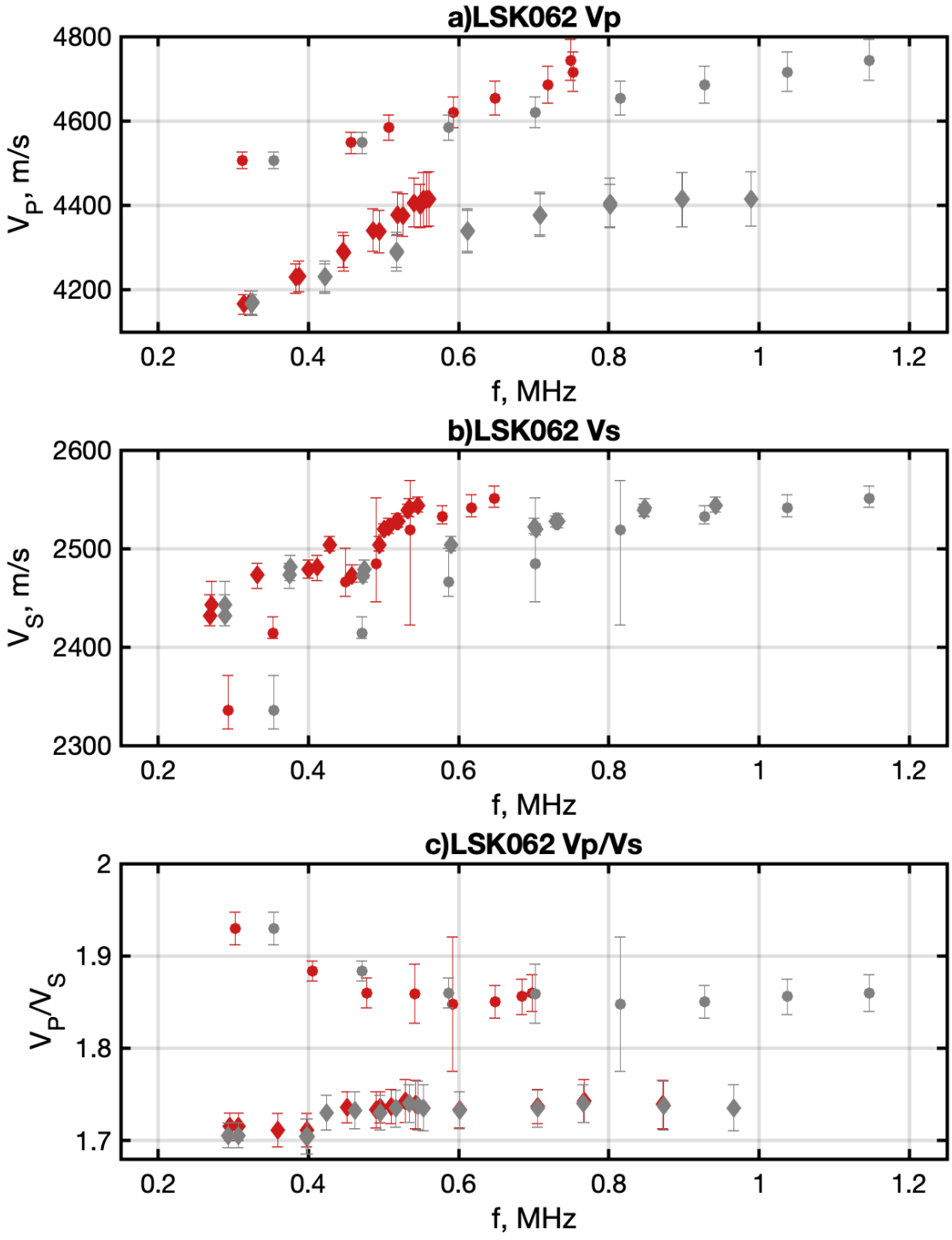


*Figure 11. Panel a and b are sample LSK062 frequency-dependent Vp and Vs, respectively. Diamonds and circles indicate laboratory and numerical measurements, respectively. Red and*

*gray markers have frequencies equal to $\bar{f}$ and $f_i$, respectively. Errorbars have magnitues equal to $\Delta V^{+,-}$. The overall range of Vp spans about 300 m/s, well above the size of the error bars. Vs velocities range span about 200 m/s. Velocities illustrate dispersive behavior where the most rapid changes occur for frequencies >0.4 MHz. Velocities as a function of frequency show that transmitted frequencies ($\bar{f}$ in red) do not exceed about 0.55 MHz. The Vp/Vs values in c) all fall above $\sqrt{2}$. In panels a and b, the frequencies are $f_i$ for the gray markers and $\bar{f}$ for the red markers. In panel c, Vp/Vs are calculated for each pair of Vp, and Vs that are measured at the same $f_i$. Vp/Vs frequencies are calculated as the average of the frequencies of point pairs. Error bars on Vp/Vs are the RMS average of the error bars on Vp and Vs point pairs.*

## 4 Discussion

Figure 12 summarizes the laboratory and numerical results reporting Vp, Vs and the frequency shift coefficient ($\Delta f$) for samples LSK068, LSK062, LSK014 and LSK050 as a function of porosity. On panel a are the absolute velocities – expressed as the average of the measurements taken across the frequency range. The rectangle heights indicate dispersion - i.e., max to min velocity across the frequency range.

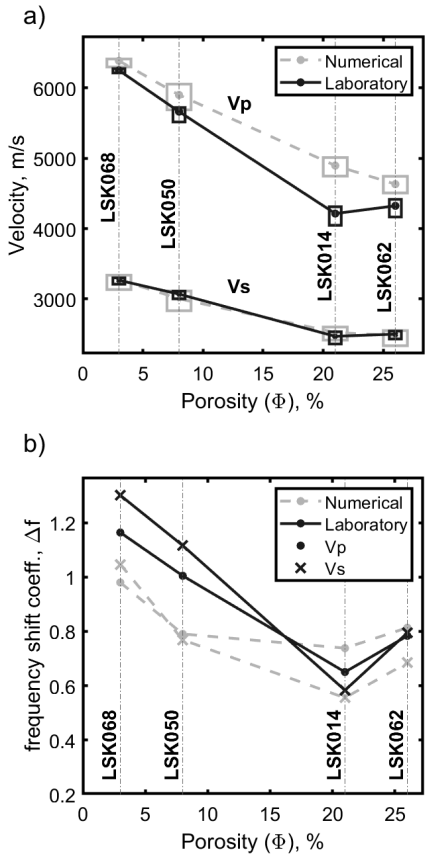


*Figure 12. Summary of the laboratory (dark line) and numerical (dashed light line) results. a) Velocities vs porosity: absolute values (dots) are calculated as the average of the measurements across the entire frequency bandwidth. The vertical size of the rectangles indicates dispersion*

595 *within the measured frequency bandwidth (i.e., ~0.3-1 MHz). Panel b shows the frequency shift*
596 *coefficient (Δf) as a function of porosity.*
597
598 The P and S velocities measured on sample LSK068 align well with the expected velocities for
599 an isotropic and homogeneous mixture of calcite crystals. For example, Peselnick & Robie
600 (1962, 1963) suggested a Vp and Vs for calcite of 6.34 and 3.27 km/s (Mavko et al., 2019). Such
601 values are similar to our laboratory measurements (Figures 6 and 7). Nevertheless, we should
602 realize that sample LSK068 has a porosity of 3% and that Peselnick & Robie measured calcite
603 properties at frequencies between 5 and 7 MHz with an estimated uncertainty up to 4%.
604 Velocities for samples LSK062, LSK014, and LSK050 are lower than those of LSK068 due to
605 their higher porosity, which is between 8 and 26% for those samples. These samples also exhibit
606 higher dispersion than sample LSK068. The dispersion magnitudes for samples LSK068,
607 LSK062, LSK014, and LSK050 are similar between the laboratory observations and the
608 numerical simulations. However, absolute values of P velocities differ where the numerical
609 velocities are larger than the laboratory ones. On the other hand, numerical and laboratory S
610 velocities are similar. Such a discrepancy could be explained by the choice of bulk and shear
611 modulus for the μCT-model phases. We assigned a shear modulus of 30 GPa to phase 2 (i.e.,
612 calcite); however, in the literature, it is common to find higher values (Simmons & Wang, 1971).
613
614 Lower laboratory velocities compared to numerical velocities could also arise from different
615 attenuation levels. We used an elastic wavefield formulation in numerical simulations, so no
616 energy was lost due to thermoelastic or slippage between mineral grains, generally termed
617 intrinsic attenuation and dispersion. The laboratory measurements are a function of some
618 intrinsic attenuation and dispersion, but the amount is unknown.
619
620 For sample LSK068 the segmentation algorithm resulted in only the presence of phase 2, so not
621 much scattering was expected and observed, and no further analysis can be conducted regarding
622 the pore size distribution (PSD). The numerical simulation performed for Vp at the lowest
623 frequency (0.3 MHz) on sample LSK068 exhibited a velocity ~100 m/s lower than the velocities
624 measured at the other frequencies (Figure 10a). As the distance between source and receivers
625 was 28.5 mm (i.e., 927 voxels), and the wavelength was 21 mm, we suggest that near field
626 effects might have biased - lowering- the velocity estimate.
627
628 Specific to sample LSK062, P- and S-wave velocities are notably slower than for LSK068.
629 Furthermore, the amount of dispersion is much greater than for LSK068, for both P and S-waves.
630 For comparison, the pore size distribution (PSD) is shown in Figure 13a. We extract three
631 scatterer sizes (ds) from the PSD corresponding to phase 0, phase 1, and phase 0 plus phase 1.
632 Each ds is a weighted mean from the distribution ranging from 0.23 to 0.52 mm. The wavelength
633 to scatterer diameter (λ/ds) parameter is plotted as a function of frequency for P and S-waves
634 (Figure 13b), and it decreases in the range ~80 to ~8 as frequency increases. Finally, Figure 13c
635 shows the velocity dispersion for P and S waves as a function λ/ds. For elastic body waves, two
636 main types of scattering are typically assumed: Mie and Rayleigh scattering (de Hoop, 1995;
637 Mavko et al., 2019; Snieder, 2002). Sample LSK014 exhibits similar velocities and an amount of
638 dispersion comparable to LSK062 for P and S waves (see supporting information) over a similar
639 frequency range (compare Figures 13c to 13f). This sample has porosity similar to LSK062 and
640 scatterer sizes (ds) ranging between 0.54 and 0.75 mm as indicated in Figure 13d. The slightly

larger porosity with respect to LSK062 can also be noticed in the μCT model (Figures 1 and 5). Consequently, λ/ds values are lower than those of sample LSK062 ranging from ~40 to ~6 (Figure 13e). Given the values of the λ/ds for samples LSK014 and LSK062, we attribute the P and S waves dispersion observed in our laboratory and numerical experiments to Rayleigh scattering. Nevertheless, a few measurements on sample LSK014 exhibit λ/ds~2π and might have been affected by Mie scattering.

Sample LSK050 presents P and S velocities similar to LSK068, justified by a lower porosity than LSK062 and LSK014. However, it exhibits an amount of dispersion comparable to or higher than LSK062 and LSK014 (see supporting information) over a similar frequency range (compare Figures 13c,f, to 13i). This sample has scatterers with sizes (ds) ranging between 0.54 and 0.95 mm as indicated in Figure 13g and the μCT model (Figures 1 and 5). The μCT model also reveals that the pore space topology is much different than samples LSK062 and LSK014 exhibiting bigger and less round pores. The presence of bigger pores is also indicated by the bimodal distribution of the PSD, presenting a peak ~2.5 mm (Figure 13g). We argue that our PSD analysis is not sophisticated enough and underestimates ds for this sample. Higher ds, in the order of a few mm, would bring the λ/ds values to ~2, suggesting that LSK050 velocities are affected by Mie scattering or fall between the Rayleigh to Mie region, where the velocities change abruptly with λ/ds (Mavko et al., 2019).

| | Sample | LSK068 | LSK062 | LSK014 | LSK050 | LSK059 |
|---|---|---|---|---|---|---|
| | **Φ (%)** | 3.0 | 26.0 | 21.0 | 8.0 | 11.0 |
| **μCT-model** | **Phase 0 (%)** | 0.0 | 2.7 | 2.9 | 0.7 | 0.6 |
| | **Phase 1 (%)** | 0.0 | 47.4 | 43.7 | 17.7 | 7.9 |
| **PSD** | **Phase 0 (%)** | 0.0 | 2.8 | 3.2 | 0.7 | 0.6 |
| | **Phase 1 (%)** | 0.0 | 52.7 | 46.7 | 21.2 | 7.6 |

*Table 3. Sample porosities (Φ), relative volumes of segmentation phases estimated from the μCT-model, and pore size distributions (PSD).*

The dispersive nature of samples LSK062, LSK014 and LSK050 is also shown by Figure 12b, where the frequency shift coefficient (*Δf)* is below that of sample LSK068 and roughly inversely proportional to porosity. For the numerical experiments on sample LSK068, *Δf* is very close to one indicating no dispersion again. On the other hand, laboratory measurements on sample LSK068 exhibit *Δf* above one, especially for Vs measurements. We argue that such an effect is

related to the tendency of the piezoelectric transducers to resonate at their nominal frequency, shifting the frequency content of the signals towards 1 MHz.

### *Other laboratory scenarios*

Laboratory settings for the work presented here included measurements at different frequencies for a constant effective - in this case, also confining - pressure on dry samples. We list here three other scenarios and the potential differences in scattering and dispersion. 1) One scenario to consider is to use dry samples for varying effective pressures and varying frequencies. As effective pressure increases, flaws, cracks, and elongated pores would tend to close. As a result, the amount of scattering and dispersion should decrease as effective pressure increases. 2) If the measurements were conducted using fluid-saturated samples but at the single benchtop effective pressure, we would expect less scattering than in the dry case. This decrease would occur because of the smaller contrast in elastic properties between the saturating fluid and the rock relative to the contrast between air and rock. However, the observed dispersion due to scattering could be small relative to the dispersion caused by one or more WIFF mechanisms. 3) Combining the first two would entail saturated-rock measurements for variable frequency and effective pressure. Again, as the effective pressure increases, small-scale features would close, so scattering would decrease. However, like in the second scenario, WIFF mechanisms would be present, whose individual and collective magnitudes could be larger than scattering effects. Along with these aspects, the rock microstructure will still control the critical frequencies at which the various dispersion mechanisms would take effect.

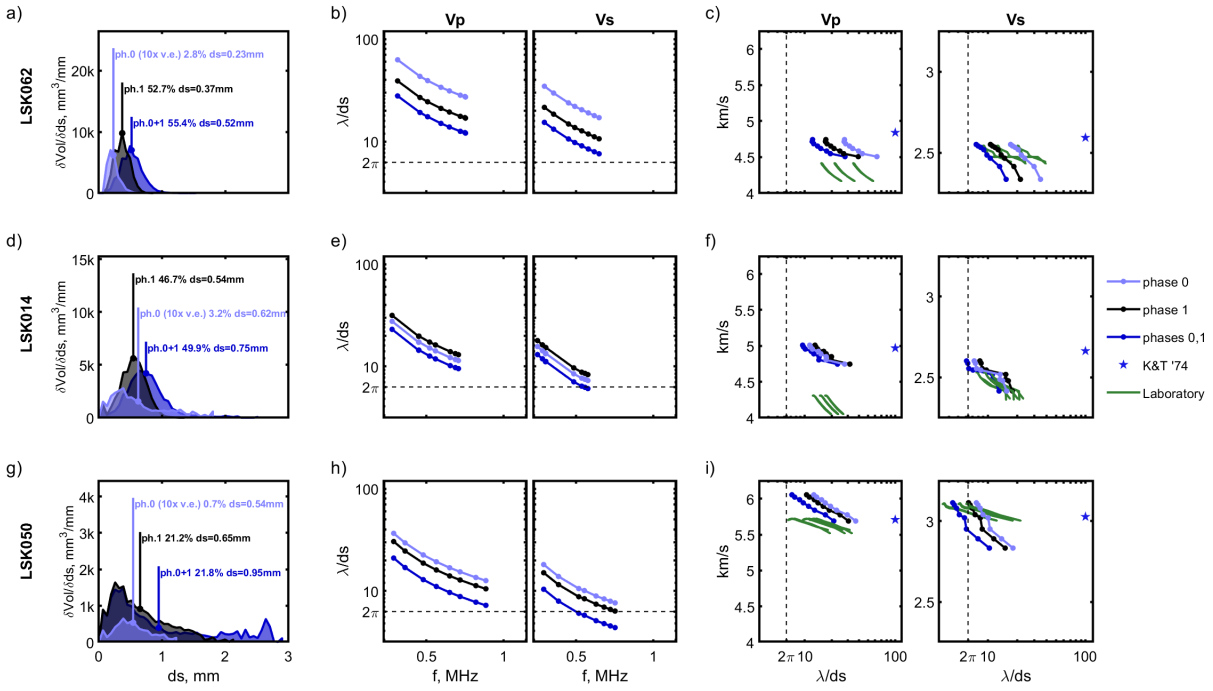


*Figure 13. Panels a, c, and g show the pore size distributions (PSD) for the samples LSK062, LSK014, and LSK050. PSDs are calculated on the μCT imagery and are expressed as* $\frac{\delta Vol}{\delta ds}$ *- i.e.,*

*the derivative of the volume of pores having a diameter below a certain ds on ds. Panels b, e, and h show the λ/ds as a function of $f_c$ for the Vp and Vs numerical experiments on LSK062, LSK014, and LSK050. These panels show that λ/ds is comprised between 2 and 100, an interval in which Rayleigh scattering is mostly active. Panels c, f, and i show the numerical and laboratory-measured velocities as a function of λ/ds. K&T '74 (blue stars) indicate velocities according to the effective medium theory proposed by Kuster & Toksöz (1974), calculated assuming the segmentation phase properties from Table 2 and quantities calculated according to the PSD (see Panels a, d, and g and Table 3).*

### *Implications*

Results from this work have three primary implications. One deals with Gassmann (1951) fluid substitution. In the practice of fluid substitution, one assumption is that the velocities of dry rocks do not vary as a function of frequency. This assumption allows for ultrasonic measurements of dry rocks to be used in low-frequency (field scale and well log) calculations for velocities of saturated rocks. If the rock microstructures, such as those in the dispersive samples shown here, cause significant scattering and velocity dispersion, then the application of fluid substitution will contain errors. The second implication falls in the purview of upscaling from the laboratory to the field scale. More specifically, the scattering observed at high frequency is due to heterogeneities comparable in size to the wavelength. At lower frequency or larger scale, heterogeneities the size of those longer wavelengths should also scatter the propagating wavefields. Geologic features that could potentially be scatterers include, but are not limited to, sedimentary and stratigraphic structures, diagenetic patterns, and volcanic deposits. An understanding of this scaling behavior would need to be studied through phenomenological viscoelastic models. The third implication pertains to laboratory ultrasonic measurements. Recorded waveforms should be analyzed routinely in terms of their spectral content. Although some mention of this effort is in the literature, most reported laboratory data are grouped by the dominant or nominal central frequency of the source input. Those source input frequencies are important to know, but the frequency content of the observed waveforms carries equally, if not more important information.

## 5 Conclusions

We conclude that the scattering of elastic waves has a first-order effect on the velocities of elastic waves in porous rocks like carbonates and that velocity variations might have reasons beyond the commonly invoked mechanisms, such as variation of pore shapes. Our measurements indicate a significant increase in the velocity of waves propagating through carbonate samples when the wavelength-to-scatterer size ratio is below $2\pi$. In the past, variations of elastic wave velocities could have been misinterpreted, and future measurements should be analyzed along with the observed dispersion and frequency shift when possible.

## Acknowledgments

We thank Ken Ikeda, Tom Hess, and Steve Grand for technical support and thorough discussions. We thank Shell International Exploration & Production Inc. for permission to publish.

## Open Research

Data are publicly available upon publication at https://doi.org/10.18738/T8/KTFFU2 or can be requested to the corresponding author.

## References

Adam, L., Batzle, M., Lewallen, K. T., & van Wijk, K. (2009). Seismic wave attenuation in carbonates. *Journal of Geophysical Research*, *114*(B6). https://doi.org/10.1029/2008JB005890

Adam, Ludmila, Batzle, M., & Brevik, I. (2006). Gassmann's fluid substitution and shear modulus variability in carbonates at laboratory seismic and ultrasonic frequencies. *GEOPHYSICS*, *71*(6), F173–F183. https://doi.org/10.1190/1.2358494

Aki, K., & Richards, P. G. (2009). *Quantitative seismology* (2. ed., corr. print). Sausalito, Calif: Univ. Science Books.

Andrä, H., Combaret, N., Dvorkin, J., Glatt, E., Han, J., Kabel, M., et al. (2013a). Digital rock physics benchmarks—Part I: Imaging and segmentation. *Computers & Geosciences*, *50*, 25–32. https://doi.org/10.1016/j.cageo.2012.09.005

Andrä, H., Combaret, N., Dvorkin, J., Glatt, E., Han, J., Kabel, M., et al. (2013b). Digital rock physics benchmarks—part II: Computing effective properties. *Computers & Geosciences*, *50*, 33–43. https://doi.org/10.1016/j.cageo.2012.09.008

Anselmetti, F. S., von Salis, G. A., Cunningham, K. J., & Eberli, G. P. (1997). Acoustic properties of Neogene carbonates and siliciclastics from the subsurface of the Florida Keys: implications for seismic reflectivity. *Marine Geology*, *144*(1–3), 9–31. https://doi.org/10.1016/S0025-3227(97)00081-9

759 Azzalini, A. (1985). A class of distributions which includes the normal ones. *Scandinavian*
760 *Journal of Statistics*, *12*, 171–178.
761 Baechle, G. T., Colpaert, A., Eberli, G. P., & Weger, R. J. (2008). Effects of microporosity on
762 sonic velocity in carbonate rocks. *The Leading Edge*, *27*(8), 1012–1018.
763 https://doi.org/10.1190/1.2967554
764 Bemer, E., Hamon, Y., & Adelinet, M. (2017). Integrated Characterization Workflow to Assess
765 Diagenesis Impact on the Petrophysical and Petroacoustic Properties of Carbonate
766 Reservoirs. In *Poromechanics VI: Proceedings of the Sixth Biot Conference on*
767 *Poromechanics* (pp. 1884–1891). Paris, France: ASCE. Retrieved from
768 https://ascelibrary.org/doi/book/10.1061/9780784480779
769 Best, A. I., McCann, C., & Sothcott, J. (1994). The relationships between the velocities,
770 attenuations and petrophysical properties of reservoir sedimentary rocks1. *Geophysical*
771 *Prospecting*, *42*(2), 151–178. https://doi.org/10.1111/j.1365-2478.1994.tb00204.x
772 Birch, F. (1960). The velocity of compressional waves in rocks to 10 kilobars: 1. *Journal of*
773 *Geophysical Research*, *65*(4), 1083–1102. https://doi.org/10.1029/JZ065i004p01083
774 Bohlen, T. (2002). Parallel 3-D viscoelastic finite difference seismic modelling. *Computers &*
775 *Geosciences*, *28*(8), 887–899. https://doi.org/10.1016/S0098-3004(02)00006-7
776 Bosellini, A., Mutti, E., & Ricci Lucchi, F. (1995). *Rocce e successioni sedimentarie* (Ristampa).
777 Torino: UTET.
778 Bourbié, T., Coussy, O., & Zinszner, B. (1987). *Acoustics of Porous Media*. Houston u.a.; Paris:
779 Gulf Publ. Co. u.a.; Ed. Technip.
780 Carpenter, B. M., Saffer, D. M., & Marone, C. (2015). Frictional properties of the active San
781 Andreas Fault at SAFOD: Implications for fault strength and slip behavior: Friction of

SAF at SAFOD. *Journal of Geophysical Research: Solid Earth*, *120*(7), 5273–5289. https://doi.org/10.1002/2015JB011963

Casteleyn, L., Robion, P., Collin, P.-Y., Menéndez, B., David, C., Desaubliaux, G., et al. (2010). Interrelations of the petrophysical, sedimentological and microstructural properties of the Oolithe Blanche Formation (Bathonian, saline aquifer of the Paris Basin). *Sedimentary Geology*, *230*(3–4), 123–138. https://doi.org/10.1016/j.sedgeo.2010.07.003

Casteleyn, L., Robion, P., David, C., Collin, P.-Y., Menéndez, B., Fernandes, N., et al. (2011). An integrated study of the petrophysical properties of carbonate rocks from the "Oolithe Blanche" formation in the Paris Basin. *Tectonophysics*, *503*(1–2), 18–33. https://doi.org/10.1016/j.tecto.2010.09.031

Clark, A. C., & Vanorio, T. (2016). The rock physics and geochemistry of carbonates exposed to reactive brines: Fluid-Rock Interaction in Carbonates. *Journal of Geophysical Research: Solid Earth*, *121*(3), 1497–1513. https://doi.org/10.1002/2015JB012445

Di Martino, M. D. P., De Siena, L., & Tisato, N. (2022). Pore Space Topology Controls Ultrasonic Waveforms in Dry Volcanic Rocks. *Geophysical Research Letters*, *49*(18), e2022GL100310. https://doi.org/10.1029/2022GL100310

Dunham, R. J. (1962). Classification of Carbonate Rocks According to Depositional Textures. *AAPG Special Volumes*, 108–121.

Eberli, G. P., Baechle, G. T., Anselmetti, F. S., & Incze, M. L. (2003). Factors controlling elastic properties in carbonate sediments and rocks. *The Leading Edge*, *22*(7), 654–660. https://doi.org/10.1190/1.1599691

803 Fabricius, I. L., Bächle, G. T., & Eberli, G. P. (2010). Elastic moduli of dry and water-saturated
804 carbonates — Effect of depositional texture, porosity, and permeability. *GEOPHYSICS*,
805 *75*(3), N65–N78. https://doi.org/10.1190/1.3374690
806 Gassmann, F. (1951). Elastic waves through a packing of spheres. *GEOPHYSICS*, *16*(4), 673–
807 685. https://doi.org/10.1190/1.1437718
808 Goldfarb, E. J., Ikeda, K., Ketcham, R. A., Prodanović, M., & Tisato, N. (2022). Predictive
809 digital rock physics without segmentation. *Computers & Geosciences*, *159*, 105008.
810 https://doi.org/10.1016/j.cageo.2021.105008
811 Gritto, R., Korneev, V. A., & Johnson, L. R. (1995). Low-frequency elastic-wave scattering by
812 an inclusion: limits of applications. *Geophysical Journal International*, *120*(3), 677–692.
813 https://doi.org/10.1111/j.1365-246X.1995.tb01845.x
814 Heydari, E. (2003). Meteoric versus burial control on porosity evolution of the Smackover
815 Formation. *AAPG Bulletin*, *87*(11), 1779–1797. https://doi.org/10.1306/07070302009
816 de Hoop, A. T. (1995). *Handbook of radiation and scattering of waves: acoustic waves in fluids,*
817 *elastic waves in solids, electromagnetic waves*. London San Diego New York [etc.]:
818 Academic press.
819 Ikeda, K., Goldfarb, E. J., & Tisato, N. (2020). Calculating Effective Elastic Properties of Berea
820 Sandstone Using the Segmentation-Less Method Without Targets. *Journal of*
821 *Geophysical Research: Solid Earth*, *125*(6). https://doi.org/10.1029/2019JB018680
822 Ikeda, K., Subramaniyan, S., Quintal, B., Goldfarb, E. J., Saenger, E. H., & Tisato, N. (2021).
823 Low-Frequency Elastic Properties of a Polymineralic Carbonate: Laboratory
824 Measurement and Digital Rock Physics. *Frontiers in Earth Science*, *9*, 628544.
825 https://doi.org/10.3389/feart.2021.628544

826 Japsen, P., Bruun, A., Fabricius, I. L., Rasmussen, R., Vejbæk, O. V., Pedersen, J. M., et al.
827 (2004). Influence of porosity and pore fluid on acoustic properties of chalk: AVO
828 response from oil, South Arne Field, North Sea. *Petroleum Geoscience*, *10*(4), 319–330.
829 https://doi.org/10.1144/1354-079303-586
830 Johnson, L. R. (2018). Scattering of elastic waves by a spheroidal inclusion. *Geophysical*
831 *Journal International*, *212*(3), 1829–1858. https://doi.org/10.1093/gji/ggx482
832 Kenter, J. A. M., Braaksma, H., Verwer, K., & van Lanen, X. M. T. (2007). Acoustic behavior of
833 sedimentary rocks: Geologic properties versus Poisson's ratios. *The Leading Edge*, *26*(4),
834 436–444. https://doi.org/10.1190/1.2723206
835 Kerimov, A., Cook, J., Lane, N., Lakshtanov, D., & Gettemy, G. (2020). Estimating dry rock
836 frame moduli of high-resolution 3D digital rock images using the contact-mechanics-
837 based effective medium approach. *GEOPHYSICS*, *85*(4), MR235–MR243.
838 https://doi.org/10.1190/geo2019-0655.1
839 Korneev, V. A., & Johnson, L. R. (1996). Scattering ofP andS waves by a spherically symmetric
840 inclusion. *Pure and Applied Geophysics*, *147*(4), 675–718.
841 https://doi.org/10.1007/BF01089697
842 Kuster, G. T., & Toksöz, M. N. (1974). VELOCITY AND ATTENUATION OF SEISMIC
843 WAVES IN TWO-PHASE MEDIA: PART I. THEORETICAL FORMULATIONS.
844 *GEOPHYSICS*, *39*(5), 587–606. https://doi.org/10.1190/1.1440450
845 Lambert, L., Durlet, C., Loreau, J.-P., & Marnier, G. (2006). Burial dissolution of micrite in
846 Middle East carbonate reservoirs (Jurassic–Cretaceous): keys for recognition and timing.
847 *Marine and Petroleum Geology*, *23*(1), 79–92.
848 https://doi.org/10.1016/j.marpetgeo.2005.04.003

849 Leger, M., & Luquot, L. (2021). Importance of Microstructure in Carbonate Rocks: Laboratory
850 and 3D-Imaging Petrophysical Characterization. *Applied Sciences*, *11*(9), 3784.
851 https://doi.org/10.3390/app11093784
852 Lozovyi, S., & Bauer, A. (2019). Velocity dispersion in rocks: A laboratory technique for direct
853 measurement of P-wave modulus at seismic frequencies. *Review of Scientific*
854 *Instruments*, *90*(2), 024501. https://doi.org/10.1063/1.5026969
855 Madonna, C., Almqvist, B. S. G., & Saenger, E. H. (2012). Digital rock physics: numerical
856 prediction of pressure-dependent ultrasonic velocities using micro-CT imaging: Digital
857 rock physics. *Geophysical Journal International*, *189*(3), 1475–1482.
858 https://doi.org/10.1111/j.1365-246X.2012.05437.x
859 Makhloufi, Y., Collin, P.-Y., Bergerat, F., Casteleyn, L., Claes, S., David, C., et al. (2013).
860 Impact of sedimentology and diagenesis on the petrophysical properties of a tight oolitic
861 carbonate reservoir. The case of the Oolithe Blanche Formation (Bathonian, Paris Basin,
862 France). *Marine and Petroleum Geology*, *48*, 323–340.
863 https://doi.org/10.1016/j.marpetgeo.2013.08.021
864 Matsushima, J., Ali, M. Y., & Bouchaala, F. (2020). Propagation of waves with a wide range of
865 frequencies in digital core samples and dynamic strain anomaly detection: carbonate rock
866 as a case study. *Geophysical Journal International*, *224*(1), 340–354.
867 https://doi.org/10.1093/gji/ggaa467
868 Mavko, G., Mukerji, T., & Dvorkin, J. (2009). *The rock physics handbook: tools for seismic*
869 *analysis of porous media* (2nd ed). Cambridge, UK ; New York: Cambridge University
870 Press.

Mavko, G., Mukerji, T., & Dvorkin, J. (2019). *The rock physics handbook* (Third edition). Cambridge, United Kingdom: Cambridge University Press.

Münch, B., & Holzer, L. (2008). Contradicting Geometrical Concepts in Pore Size Analysis Attained with Electron Microscopy and Mercury Intrusion. *Journal of the American Ceramic Society*, *91*(12), 4059–4067. https://doi.org/10.1111/j.1551-2916.2008.02736.x

Nader, F. H., Champenois, F., Barbier, M., Adelinet, M., Rosenberg, E., Houel, P., et al. (2016). Diagenetic effects of compaction on reservoir properties: The case of early callovian "Dalle Nacrée" formation (Paris basin, France). *Journal of Geodynamics*, *101*, 5–29. https://doi.org/10.1016/j.jog.2016.05.010

Neveux, L., Grgic, D., Carpentier, C., Pironon, J., Truche, L., & Girard, J. P. (2014). Experimental simulation of chemomechanical processes during deep burial diagenesis of carbonate rocks: EXPERIMENTATION ON LIMESTONE DIAGENESIS. *Journal of Geophysical Research: Solid Earth*, *119*(2), 984–1007. https://doi.org/10.1002/2013JB010516

Peselnick, L., & Outerbridge, W. F. (1961). Internal friction in shear and shear modulus of Solenhofen limestone over a frequency range of $10^{7}$ cycles per second. *Journal of Geophysical Research*, *66*(2), 581. https://doi.org/10.1029/JZ066i002p00581

Peselnick, L., & Robie, R. A. (1962). Elastic Constants of Calcite. *Journal of Applied Physics*, *33*(9), 2889–2892. https://doi.org/10.1063/1.1702572

Peselnick, L., & Robie, R. A. (1963). Elastic Constants of Calcite. *Journal of Applied Physics*, *34*(8), 2494–2495. https://doi.org/10.1063/1.1702777

892 Pimienta, L., Fortin, J., & Guéguen, Y. (2014). Investigation of elastic weakening in limestone
893 and sandstone samples from moisture adsorption. *Geophysical Journal International*,
894 *199*(1), 335–347. https://doi.org/10.1093/gji/ggu257
895 Quan, Y., & Harris, J. M. (1997). Seismic attenuation tomography using the frequency shift
896 method. *GEOPHYSICS*, *62*(3), 895–905. https://doi.org/10.1190/1.1444197
897 Rafavich, F., Kendall, C. H. St. C., & Todd, T. P. (1984). The relationship between acoustic
898 properties and the petrographic character of carbonate rocks. *GEOPHYSICS*, *49*(10),
899 1622–1636. https://doi.org/10.1190/1.1441570
900 Rasolofosaon, P., & Zinszner, B. (2003). Petroacoustic Characterization of Reservoir Rocks for
901 Seismic Monitoring Studies. Laboratory Measurement of Hertz and Gassmann
902 Parameters. *Oil & Gas Science and Technology*, *58*(6), 615–635.
903 https://doi.org/10.2516/ogst:2003043
904 Regnet, J. B., Robion, P., David, C., Fortin, J., Brigaud, B., & Yven, B. (2015). Acoustic and
905 reservoir properties of microporous carbonate rocks: Implication of micrite particle size
906 and morphology. *Journal of Geophysical Research: Solid Earth*, *120*(2), 790–811.
907 https://doi.org/10.1002/2014JB011313
908 Regnet, J. B., David, C., Fortin, J., Robion, P., Makhloufi, Y., & Collin, P. Y. (2015). Influence
909 of microporosity distribution on the mechanical behavior of oolithic carbonate rocks.
910 *Geomechanics for Energy and the Environment*, *3*, 11–23.
911 https://doi.org/10.1016/j.gete.2015.07.002
912 Regnet, J. B., David, C., Robion, P., & Menéndez, B. (2019). Microstructures and physical
913 properties in carbonate rocks: A comprehensive review. *Marine and Petroleum Geology*,
914 *103*, 366–376. https://doi.org/10.1016/j.marpetgeo.2019.02.022

915 Regnet, J.-B., Fortin, J., Nicolas, A., Pellerin, M., & Guéguen, Y. (2019). Elastic properties of
916 continental carbonates: From controlling factors to an applicable model for acoustic-
917 velocity predictions. *GEOPHYSICS*, *84*(1), MR45–MR59.
918 https://doi.org/10.1190/geo2017-0344.1
919 Richards, P. G., & Menke, W. (1983). The apparent attenuation of a scattering medium. *Bulletin*
920 *of the Seismological Society of America*, *73*(4), 1005–1021.
921 https://doi.org/10.1785/BSSA0730041005
922 Røgen, B., Fabricius, I. L., Japsen, P., Hoier, C., Mavko, G., & Pedersen, J. M. (2005).
923 Ultrasonic velocities of North Sea chalk samples: influence of porosity, fluid content and
924 texture. *Geophysical Prospecting*, *53*(4), 481–496. https://doi.org/10.1111/j.1365-
925 2478.2005.00485.x
926 Saenger, E. H., Krüger, O. S., & Shapiro, S. A. (2004). Numerical considerations of fluid effects
927 on wave propagation: Influence of the tortuosity: FLUID EFFECTS ON WAVE
928 PROPAGATION. *Geophysical Research Letters*, *31*(21), n/a-n/a.
929 https://doi.org/10.1029/2004GL020970
930 Saenger, Erik H., & Bohlen, T. (2004). Finite-difference modeling of viscoelastic and anisotropic
931 wave propagation using the rotated staggered grid. *GEOPHYSICS*, *69*(2), 583–591.
932 https://doi.org/10.1190/1.1707078
933 Saenger, Erik H., Vialle, S., Lebedev, M., Uribe, D., Osorno, M., Duda, M., & Steeb, H. (2016).
934 Digital carbonate rock physics. *Solid Earth*, *7*(4), 1185–1197. https://doi.org/10.5194/se-
935 7-1185-2016
936 Saxena, N., Hofmann, R., Hows, A., Saenger, E. H., Duranti, L., Stefani, J., et al. (2019). Rock
937 compressibility from microcomputed tomography images: Controls on digital rock

simulations. *GEOPHYSICS*, *84*(4), WA127–WA139. https://doi.org/10.1190/geo2018-0499.1

Simmons, G., & Wang, H. (1971). *Single crystal elastic constants and calculated aggregate properties: a handbook* (2d ed). Cambridge, Mass: M.I.T. Press.

Snieder, R. (2002). General Theory of Elastic Wave Scattering. In *Scattering* (pp. 528–542). Elsevier. https://doi.org/10.1016/B978-012613760-6/50027-9

Subramaniyan, S., Quintal, B., Tisato, N., Saenger, E. H., & Madonna, C. (2014). An overview of laboratory apparatuses to measure seismic attenuation in reservoir rocks: Apparatuses to measure seismic attenuation. *Geophysical Prospecting*, *62*(6), 1211–1223. https://doi.org/10.1111/1365-2478.12171

Szewczyk, D., Bauer, A., & Holt, R. M. (2016). A new laboratory apparatus for the measurement of seismic dispersion under deviatoric stress conditions: Apparatus for seismic dispersion. *Geophysical Prospecting*, *64*(4), 789–798. https://doi.org/10.1111/1365-2478.12425

Tisato, N., & Marelli, S. (2013). Laboratory measurements of the longitudinal and transverse wave velocities of compacted bentonite as a function of water content, temperature, and confining pressure: ELASTIC PROPERTIES OF BENTONITE. *Journal of Geophysical Research: Solid Earth*, *118*(7), 3380–3393. https://doi.org/10.1002/jgrb.50252

Tisato, N., Madonna, C., & Saenger, E. H. (2021). Attenuation of Seismic Waves in Partially Saturated Berea Sandstone as a Function of Frequency and Confining Pressure. *Frontiers in Earth Science*, *9*, 641177. https://doi.org/10.3389/feart.2021.641177

Toksöz, M. N., Johnston, D. H., & Society of Exploration Geophysicists (Eds.). (1981). *Seismic wave attenuation*. Tulsa, Okla: Society of Exploration Geophysicists.

961 Verwer, K., Braaksma, H., & Kenter, J. A. (2008). Acoustic properties of carbonates: Effects of
962 rock texture and implications for fluid substitution. *GEOPHYSICS*, *73*(2), B51–B65.
963 https://doi.org/10.1190/1.2831935
964 Verwer, K., Eberli, G., Baechle, G., & Weger, R. (2010). Effect of carbonate pore structure on
965 dynamic shear moduli. *GEOPHYSICS*, *75*(1), E1–E8. https://doi.org/10.1190/1.3280225
966 Walsh, J. B. (1966). Seismic wave attenuation in rock due to friction. *Journal of Geophysical*
967 *Research*, *71*(10), 2591–2599. https://doi.org/10.1029/JZ071i010p02591
968 Wang, Z. (1997). *Seismic Properties of Carbonate Rocks*. (I. Palaz & K. J. Marfurt, Eds.) (Vol.
969 Carbonate Seismology). Society of Exploration Geophysicists.
970 https://doi.org/10.1190/1.9781560802099
971 Weger, R. J., Eberli, G. P., Baechle, G. T., Massaferro, J. L., & Sun, Y.-F. (2009). Quantification
972 of pore structure and its effect on sonic velocity and permeability in carbonates. *AAPG*
973 *Bulletin*, *93*(10), 1297–1317. https://doi.org/10.1306/05270909001
974 Winkler, K., Nur, A., & Gladwin, M. (1979). Friction and seismic attenuation in rocks. *Nature*,
975 *277*(5697), 528–531. https://doi.org/10.1038/277528a0
976 Winkler, K. W., & Nur, A. (1982). Seismic attenuation: Effects of pore fluids and frictional-
977 sliding. *GEOPHYSICS*, *47*(1), 1–15. https://doi.org/10.1190/1.1441276
978

# Scattering and Frequency Effects on Ultrasonic Velocities of Carbonates

**Nicola Tisato[1], Kyle T. Spikes[1], Nishank Saxena[2], Ronny Hofmann[2]**

[1]Department of Geological Sciences, Jackson School of Geosciences, The University of Texas at Austin

[2]Shell International Exploration & Production, Houston, TX

Corresponding author: Nicola Tisato (nicola.tisato@jsg.utexas.edu)

## Supporting information

Part of the calibration process is to determine and transfer function of the transducers that we used in the experiments. The experiments involved the use of two P and two S transducers, and their magnitude transfer functions are shown in Figure S1. Time delays in the experimental setup were determined from travel time measurements of stainless steel standards. Those measurements resulted in empirically derived functions for P (Figure S2a) and S (Figure S2b) waves.

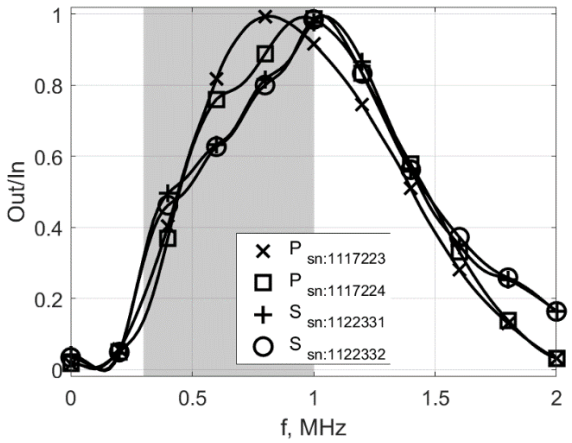


*Figure S1. Magnitude of the transfer functions of the four transducers (two P and two S) used in this study.*

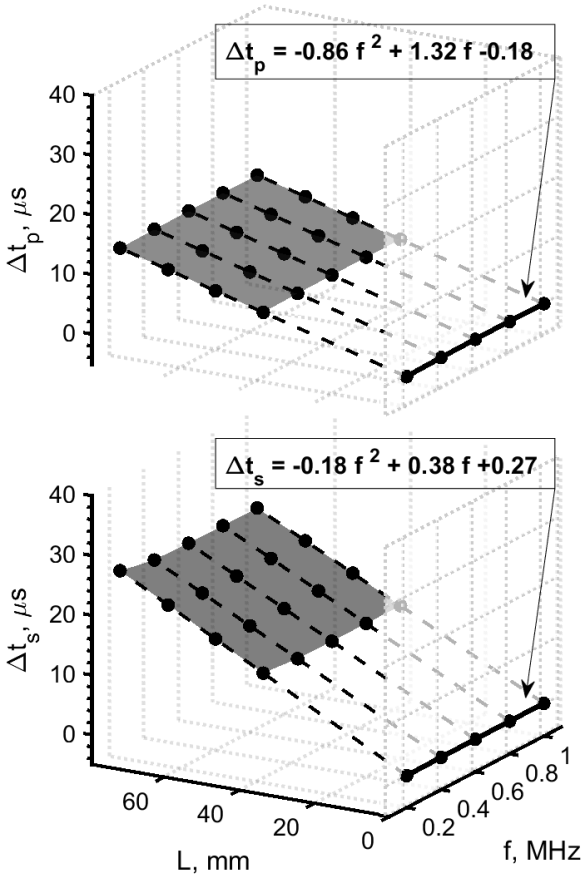


*Figure S2. Calibration data and fitting curves providing the delays ($\Delta t_p$ and $\Delta t_s$) in microseconds as a function of frequency (f) in MHz.*

Figures S3–S5 contain frequency-dependent velocities and Vp/Vs values for samples LSK014, LSK050, and LSK059. Laboratory and numerical values are included for LSK014 and LSK050 but only laboratory values for LSK059. All three samples exhibit dispersion well beyond the error bars.

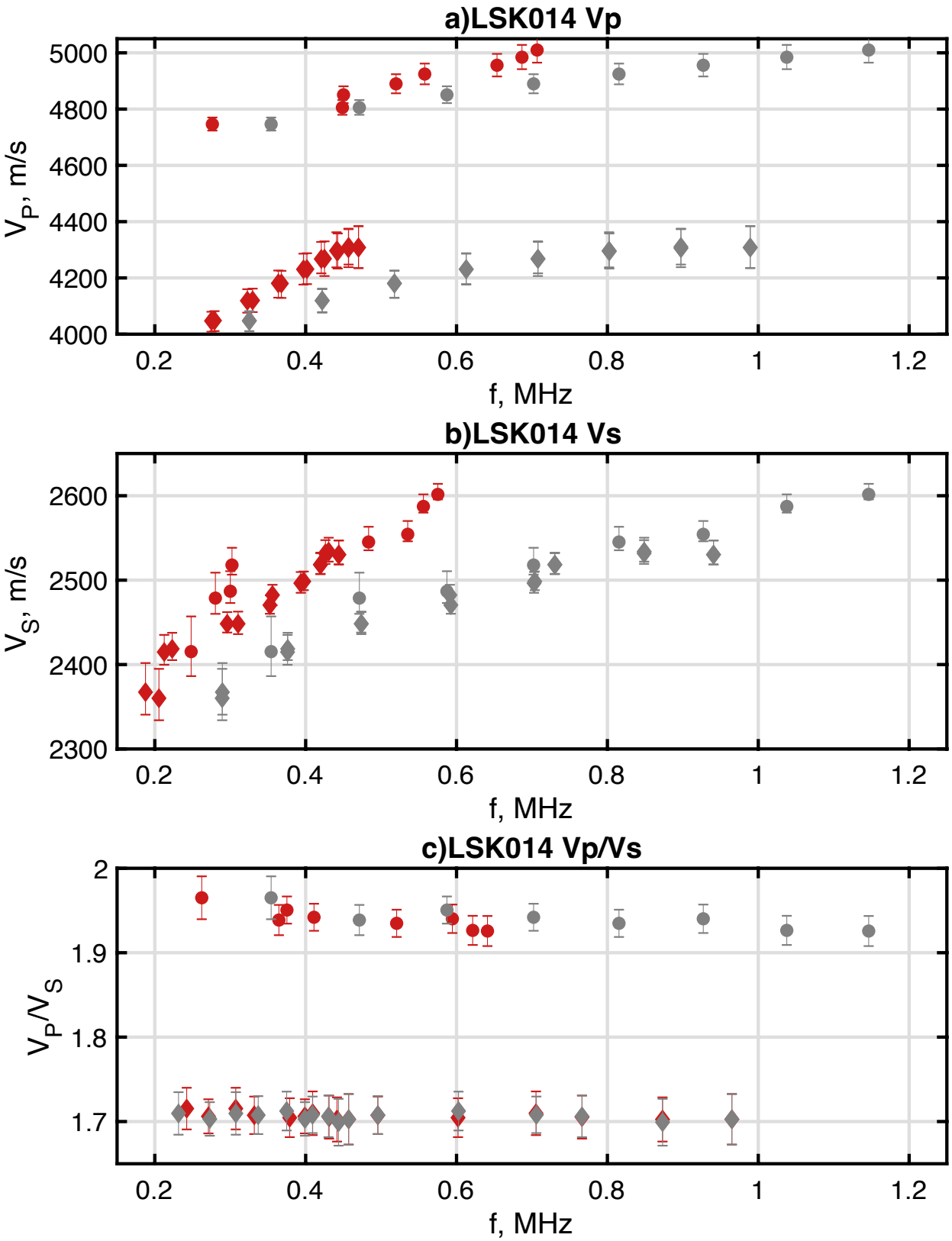


*Figure S3. Panel a and b are sample LSK014 frequency-dependent Vp and Vs, respectively. Diamonds and circles indicate laboratory and numerical measurements, respectively. Red and gray markers have frequencies equal to $f_o$ and $f_i$, respectively. Errorbars have magnitues equal*

34 *to $\Delta V^{+,-}$. The overall Vp and Vs ranges are several hundred m/s for both laboratory and*
35 *numerical experiments. Lastly in panel c are the frequency-dependent Vp to Vs ratios (Vp/Vs)*
36 *that are calculated for each pair of Vp and Vs points measured the same $f_i$. Vp/Vs frequencies*
37 *are calculated as the average of the frequencies of point pairs. Error bars on Vp/Vs are the RMS*
38 *average of the error bars on Vp and Vs point pairs.*

39

40

41

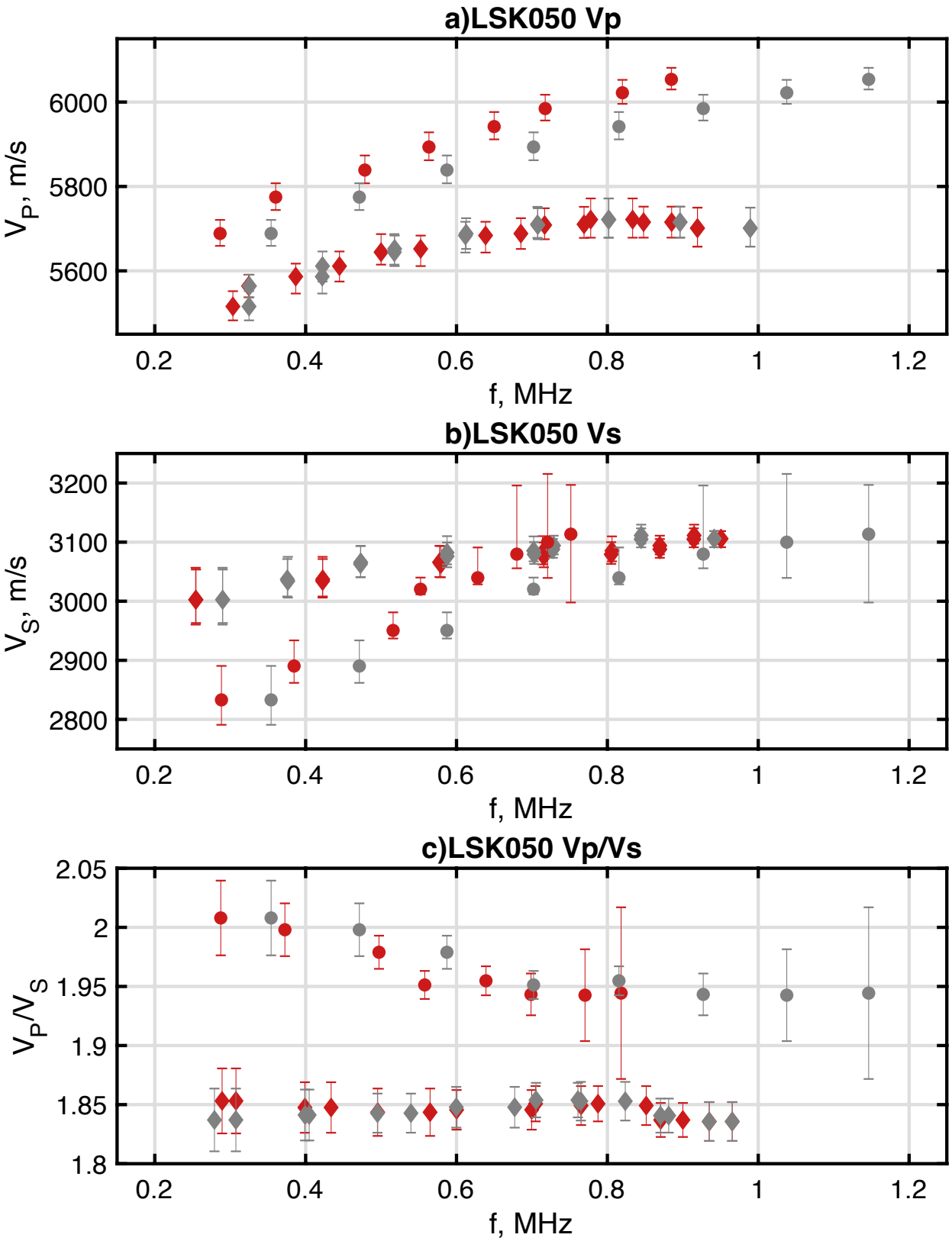


*Figure S4. Panel a and b are sample LSK050 frequency-dependent Vp and Vs, respectively, for laboratory measurements and numerical simulations. Red and gray markers have frequencies equal to $f_o$ and $f_i$, respectively. Errorbars have magnitues equal to $\Delta V^{+,-}$. The overall velocity*

*range is about 300 m/s for both laboratory and numerical experiments. Lastly in panel c are the frequency-dependent Vp to Vs ratios (Vp/Vs) that are calculated for each pair of Vp and Vs points measured the same $f_i$. Vp/Vs frequencies are calculated as the average of the frequencies of point pairs. Error bars on Vp/Vs are the RMS average of the error bars on Vp and Vs point pairs.*

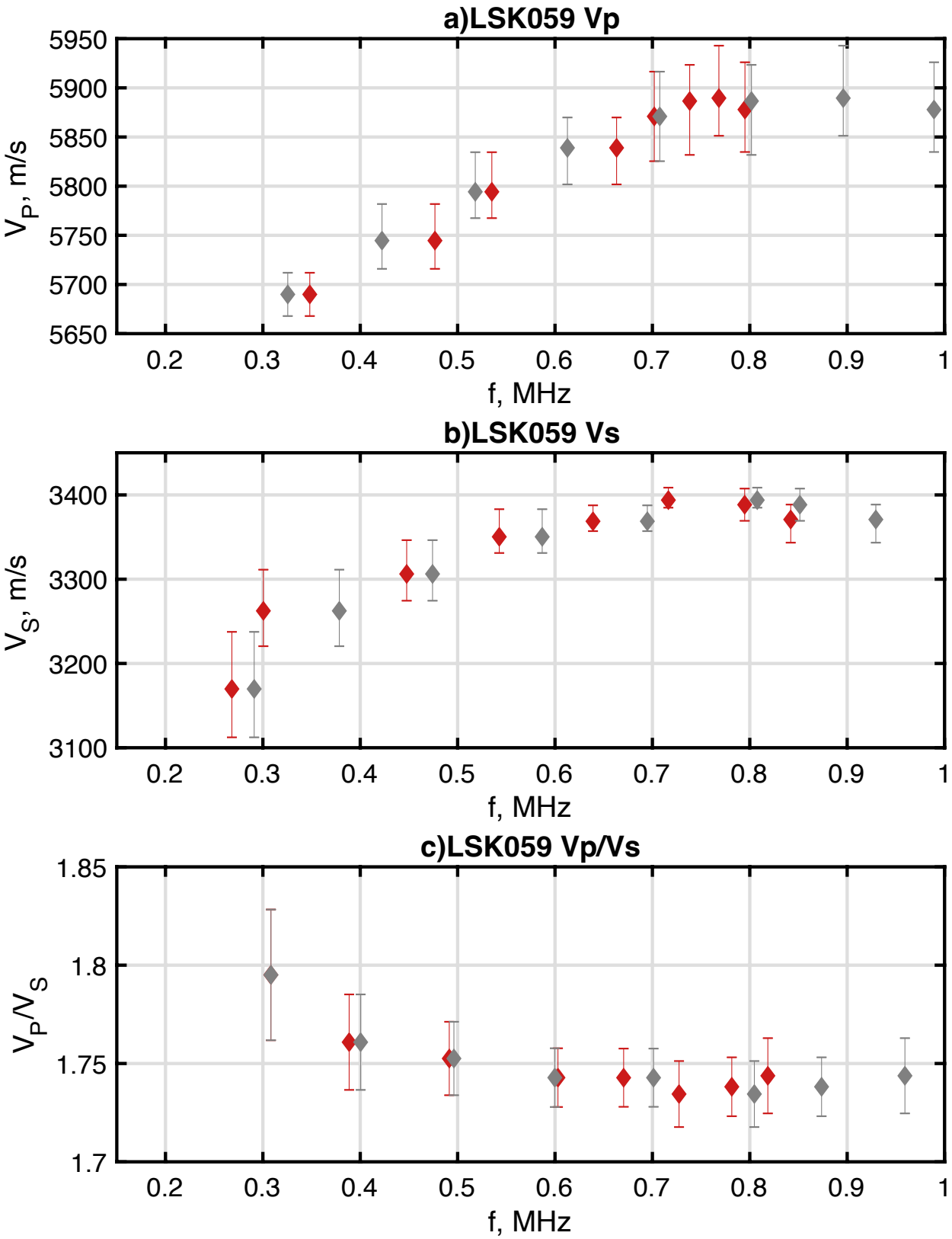


*Figure S5. Panel a and b are sample LSK059 frequency-dependent Vp and Vs, respectively. Laboratory measurements are displayed. Red and gray markers have frequencies equal to $f_o$ and $f_i$, respectively. Errorbars have magnitues equal to $\Delta V^{+,-}$. The overall velocity range is about*

57 *300 m/s for both Vp and Vs. Lastly in panel c are the frequency-dependent Vp to Vs ratios*
58 *(Vp/Vs) that are calculated for each pair of Vp and Vs points measured the same $f_i$. Vp/Vs*
59 *frequencies are calculated as the average of the frequencies of point pairs. Error bars on Vp/Vs*
60 *are the RMS average of the error bars on Vp and Vs point pairs.*

61